THE ASTROPHYSICAL JOURNAL, 486:550–570, 1997 September 1

THE HANLE EFFECT AS A DIAGNOSTIC OF MAGNETIC FIELDS IN STELLAR ENVELOPES. I. THEORETICAL RESULTS FOR INTEGRATED LINE PROFILES

R. IGNACE,[1] K. H. NORDSIECK, AND J. P. CASSINELLI
Department of Astronomy, University of Wisconsin, 5534 Sterling Hall, 475 North Charter Street, Madison, WI 53706-1582
Received 1997 January 10; accepted 1997 April 4

ABSTRACT

The Hanle effect concerns the modification of polarized resonance-line scattering by magnetic fields; thus, it can be used as a diagnostic of stellar magnetic fields. The Hanle effect has been used to determine the field strength and distribution of magnetic structures present in prominences of the Sun. To investigate its potential use in stellar astronomy, the simplified case of an optically thin axisymmetric ring illuminated by a stellar point source is considered. The results are then used to derive the polarization from polar plumes, equatorial disks, and spherical shells. The integrated line polarization is calculated for axisymmetric rings with a variety of magnetic field orientations, and in every case the polarization is proportional to $\sin^2 i$ (where i is the viewing inclination), just as in the zero field case. It is also found that the Hanle effect can significantly alter the integrated line polarization. In some cases the position angle of the polarization in the line can be rotated by 90° relative to the zero field case. We consider the Hanle effect as a possible diagnostic of magnetic fields in stellar winds with prominent ultraviolet and visible resonance lines. For these lines the diagnostic has sensitivity in the range of 1–1000 G. The Zeeman effect is not normally applicable for diagnosing magnetic fields in stellar winds in the subkilogauss range; thus, the Hanle effect should provide an especially useful new method of determining magnetic fields in stars other than the Sun. Possibilities for measuring the fields in early-type stars using ultraviolet observations is discussed.

Subject headings: line: formation — polarization — stars: magnetic fields — Sun: magnetic fields — Sun: prominences

1. INTRODUCTION

Given a known magnetic field geometry, the Hanle effect has been used by atomic physicists to measure the lifetimes of atomic levels. However, in astronomical applications the transition lifetimes are taken as known, and the Hanle effect may be used to derive information about the magnetic field properties in the line formation region. The purpose of this paper is to explore the use of the Hanle effect in stellar astronomy in order to ascertain the presence and distribution of magnetic fields in circumstellar envelopes.

Stellar magnetic fields can have many interesting (even dominant) effects on stellar outflows. Magnetic fields can accelerate a wind through Alfvén wave driving (Cassinelli 1982; dos Santos, Jatenco-Pereira, & Opher 1993; Lou & Rosner 1994) or by the magnetic rotator mechanism (Weber & Davis 1967; Poe, Friend, & Cassinelli 1989). The fields may also shape the wind geometry (Shore 1987; Chevalier & Luo 1994). The magnetic fields can affect the mass-loss rate and velocity distribution of outflows and lead to significant deviations from spherical symmetry. Although the mechanisms by which outflows can be driven or influenced by magnetic fields has been widely studied from a theoretical point of view, there is relatively little observational data regarding the fields. A few exceptions include the Bp, Bm, Ap, and Am stars for which Zeeman measurements exist (Landstreet et al. 1989; Babel, North, & Queloz 1995), and flaring stars for which fields are postulated as the only plausible mechanism (Haisch & Schmidt 1996; Johns-Krull & Valenti 1996). White dwarfs and neutron stars are known to possess strong magnetic fields, with surface strengths of order 10^6–10^8 and 10^8–10^{13} G, respectively (Chanmugam 1992); these, too, are measured using the Zeeman effect.

Diagnosing the geometry and strength of stellar magnetic fields by the Zeeman effect can be difficult unless the aspect geometry is particularly simple, because in complicated geometries there can be significant cancellation of the polarization between the Zeeman components. To infer the magnetic field strength from magnetic broadening in the spectral lines from distant stars typically requires rather large magnetic fields of kilogauss strength or greater, yet magnetic fields of only 1–100 G might lead to interesting dynamical effects in many stellar winds.

The Hanle effect (Hanle 1923; Weiskopf 1931; Mitchell & Zemansky 1934; House 1970; Stenflo 1994) provides a diagnostic of magnetic fields that operates at a lower range of field strengths than does the Zeeman effect. The Hanle effect concerns the modification of the polarizing effects of resonance-line scattering by a magnetic field. An excellent reference detailing the application of the Hanle effect in various areas of physics has been compiled by Moruzzi & Strumia (1991).

In astronomy the Hanle effect has been used to diagnose magnetic fields in solar prominences (Leroy 1985; Bommier, Leroy, & Sahal-Bréchot 1986; Landi Degl'Innocenti 1990; Bommier et al. 1994) and the upper solar atmosphere (Stenflo 1982; Sahal-Bréchot, Malinovsky, & Bommier 1986; Faurobert-Scholl 1992), and as a diagnostic of solar turbulent field strengths (Stenflo 1982; Faurobert-Scholl 1993). The current status of the theory and observations of the Hanle effect in solar studies is discussed in several contributions of a workshop on solar polarization (Stenflo & Nagendra 1996).

There are important differences in the analysis of light from distant stars versus that of the Sun. Even if the field strengths and geometries for some stars should happen to bear some resemblance to that of the Sun, it is the specific intensity of the radiation field that is observed in the case of

[1] Now at Department of Physics and Astronomy, University of Glasgow, Glasgow G12 8QQ, Scotland, UK; rico@astro.gla.ac.uk.

the Sun, whereas in the stellar case it is the net flux as integrated over the entire projected area of the star and its envelope that is observed. Thus, the viability of the Hanle effect as a magnetic diagnostic for distant stars is not obvious a priori. Clearly, in the stellar case we must be concerned about the entire geometrical structure of the star as seen from the observer's perspective. This problem not only arises in our study of the Hanle effect, but is also important in the simpler but related case of continuum polarization produced by electron scattering. We therefore comment on the methods and results of polarization studies for stars.

For hot stars continuum polarization arises from the scattering of light by free electrons. Both the theory and observations of polarization induced by electron scattering in stars and active galactic nuclei are active areas of research (e.g., Kartje 1995; Wood et al. 1996; Hillier 1996; Höflich et al. 1996). A common aspect shared by all of these different investigations is that the polarization of the flux from an unresolved object results only if there is an anisotropic distribution of either the electron scatterers or the radiation field.

In a seminal paper concerning the polarization from electron scattering envelopes, Brown & McLean (1977) developed a particularly effective way of understanding how a net polarization may result by considering the scattering of light in an axisymmetric ring of electrons illuminated by a point source. They found the following results for an optically thin electron scattering envelope: (1) the net observed polarization is proportional to $\sin^2 i$, where i is the line-of-sight viewing inclination, and (2) the magnitude of the polarization depends on a ratio of two volume integrals over the density structure. Cassinelli, Nordsieck, & Murison (1987) found that the magnitudes of the predicted polarization could be brought much closer to those of the observations by replacing the point-source approximation with a spherical central star of finite radius. Their modifications are known as the "finite disk correction" factor.

Subsequently, there have been numerous studies of the polarization arising from electron scattering in stellar envelopes. A short list of examples includes the effects of stellar occultation (Fox 1991), the effects of electron scattering for line profiles (Wood & Brown 1994a, 1994b), the effects of gravity darkening (Bjorkman & Bjorkman 1994), and the effects of prescattering attenuation (Wood & Bjorkman 1995). Additionally, Whitney (1991a, 1991b) has studied the observational consequences of strong magnetic fields for the polarization of electron scattering envelopes, with applications to white dwarf stars.

The Brown & McLean (1977) method of treating a ring of scatterers has ultimately led to a rather sophisticated level of understanding electron scattering effects in stellar envelopes. We have decided to use their basic approach as a guide for the present analysis of the Hanle effect. In addition to their description of the axisymmetric geometry, we have the additional complication of having to describe the wide range of magnetic field geometries and strengths that can occur in stellar envelopes. In this paper emphasis is given to simple axially symmetric geometries for both the stellar magnetic field and the envelope density distribution.

An outline of the paper is as follows. In § 2, we discuss resonance-line scattering and introduce the Hanle effect. Results for axisymmetric envelopes are given in § 3, in which the simplified cases of rings, sectors of revolution, and spheres are considered. In § 4, the classes of stars for which our results might be applicable are discussed, and a procedure for using the Hanle diagnostic with observations is developed. The major results of the paper are then summarized in § 5. Finally, in the Appendix, the general Hanle scattering phase matrix is presented.

2. BASIC DESCRIPTION OF THE HANLE EFFECT

The basic properties of the Hanle effect can be derived from the classical description of a damped oscillator in a magnetic field (Corney 1977). The expressions for deriving the Hanle effect are given in Stenflo (1994). Here we briefly review the properties of resonance-line scattering with and without a magnetic field. Stokes parameters are introduced, and a useful representation of the Hanle effect in terms of electric dipoles is presented.

2.1. *Resonance-Line Scattering in a Magnetic Field*

The first observations of resonance-line scattering polarization in the Sun were performed by Redman (1941) using the Ca I 4227 line. Bracketing that work are two papers by Zanstra (1941a, 1941b) describing, first, the basic theory of line polarization and, second, the effects of collisional damping for reducing the polarization to values consistent with those observed by Redman. More recently, investigations and applications of resonance-line scattering polarization for interpreting observations from the Sun have been discussed by Stenflo & Stenholm (1976) and Dumont et al. (1977), who considered non-LTE line formation in a plane-parallel atmosphere. In contrast to the solar case, there have been few observational studies of resonance-line polarization from other stars. Yet the theory of resonance-line polarization from distant stars has been developed extensively. For example, Nagendra (1988) investigated the resonance-line polarization arising from extended spherical atmospheres, to be used for studying resolved stars. McKenna (1981, 1984, 1985) studied the consequences of various frequency redistributions for the transfer of polarized radiation in spectral lines. Jeffery (1988, 1989) treated the case of resonance-line polarization in moving atmospheres, employing the Sobolev approximation. However, magnetic fields, and more specifically the Hanle effect, have not been considered in any of these stellar studies. Before describing the Hanle effect for resonance-line scattering, we first describe the case of no magnetic fields.

2.1.1. *Comparison of Resonance-Line Scattering with Electron Scattering*

In discussing resonance-line scattering without magnetic fields, comparisons are made with the more familiar process of electron scattering. Since we have an interest in the winds from early-type stars, most of the discussion is given in that context. There are four major differences between resonance-line scattering and electron scattering. (1) The line cross sections can be much larger (by several orders of magnitude) than the Thomson cross section for free electrons. Whereas the Thomson cross section $\sigma_T = 6.6 \times 10^{-25}$ cm^2, a strong UV resonance line may have a cross section as large as 10^{-16} cm^2 or more. (2) The number density of ions, n_i, that produce the line can be very different from the electron number density, n_e. In most hot stars, the dominant source of electrons come from ionized hydrogen; however, the ion density depends on the elemental abundance $\mathscr{A}_E$ of the atomic species and the ionization fraction

q_i of the ion stage of interest; hence, n_i can be smaller than n_e by several orders of magnitude. (3) The line scattering is frequency dependent, whereas electron scattering is gray. (4) Lastly, the line scattering phase function, which determines the angular distribution of the scattered radiation, includes an isotropic component in addition to the Rayleigh phase function, whereas electron scattering has a Rayleigh distribution of scattering only.

Attention is drawn to this fourth point, because it accounts for differences in the polarization that arises from a single atom versus that of a single electron. For resonance-line scattering, the contributions of Rayleigh and isotropic components are given by weights that are determined by the angular momentum quantum number j of the lower level and the Δj of the transition (Chandrasekhar 1960). As in Chandrasekhar, we define E_1 to be the weight (between 0 and 1) for the Rayleigh contribution, and $E_2 = 1 - E_1$ to be the weight for the isotropic part. The transfer of circular polarization is decoupled from that of the linearly polarized signal (just as is the case for nonmagnetic electron scattering), so another weight E_3 is used for circular polarization. The value of E_3 is also between 0 and 1. The polarized light results only from the Rayleigh contribution; therefore, the isotropic contribution acts to dilute the polarization relative to the pure Rayleigh scattering case. For the scattering of unpolarized light by a free electron through a right angle, the observed polarization would be $p = 100\%$. Given the same scattering geometry, the observed polarization from resonance-line scattering by a single atom would be $p = (100\%) \times E_1/(4 - E_1)$, which for $E_1 = 1$ recovers $p = 100\%$ as expected. In the case common to most stellar contexts, the polarized flux arises from the scattered light, but the unpolarized flux is dominated by direct starlight. In this limit the observed polarization is directly proportional to E_1. Chandrasekhar (1960) tabulates formulae for computing the weights E_1, E_2, and E_3 as a function of j and Δj (see his Table II).

2.1.2. *Comparison of the Hanle Effect to the Zeeman Effect*

The Hanle effect concerns the polarization arising from resonance-line scattering in the presence of "weak" magnetic fields. The effect applies when the magnetic sublevels of a line transition are sufficiently close in frequency that the natural line widths of the sublevels overlap significantly. As a consequence, quantum mechanical coherences exist that produce an interference between the polarized line components, resulting in changes of the polarization of the scattered light (House 1970). At larger field strengths, the sublevels will be distinctly separated, and the Zeeman effect will dominate over the Hanle effect, because the phase coherences are lost. Denoting Δv_Z as $v - v_0$ for the Zeeman splitting and Δv_N as the natural line width, Table 1 summarizes the different observational properties of the Zeeman and Hanle effects. Note especially that for whole star observations, the Hanle effect will typically be sensitive to much weaker field strengths than will be the Zeeman effect. Also, the Zeeman effect is usually employed in lines at IR wavelengths, because of the λ^2 dependence of Zeeman, but the field sensitivities given in Table 1 for the Hanle effect apply to strong resonance lines at UV and optical wavelengths.

As Table 1 indicates, it is the Zeeman shift relative to the natural line width that determines whether the Zeeman effect or the Hanle effect will be dominant. The Zeeman splitting is related to the Larmor precession frequency, ω_L, and the natural line width is related to the radiative transition rate, A_{ul}, for the spontaneous decay of an electron from level u to l. It is useful to consider the ratio

$$\frac{\omega_L}{A_{ul}} = \frac{eB}{2m_e cA_{ul}} \sim \frac{B}{110A_9}, \tag{1}$$

where $A_9 = A_{ul}/10^9$ Hz and other quantities are expressed in cgs units. We will show that the Hanle effect is most useful for determining the strength of the magnetic field when $\omega_L \sim A_{ul}$; thus, in the case of strong resonance lines, the Hanle effect will be sensitive to fields of order 100 G. Using equation (1), the Hanle effect can be interpreted in the context of the classical atomic oscillator model.

Suppose that an atom has been excited by light that is completely polarized. The corresponding classical description would be a one-dimensional damped oscillator, with a damping time of $1/A_{ul}$. Further suppose that a magnetic field exists perpendicular to the motion of the atomic oscillator. The atomic oscillator will begin to precess because of the magnetic field being transverse to the electron motion. Figure 1 shows the electron motion and observed intensities for three cases of ω_L/A_{ul}. If $\omega_L/A_{ul} \ll 1$, then the radiative rate is so large (or the magnetic field so weak) that the Larmor precession of the classical oscillator is completely negligible, and there is essentially no Hanle effect. This means that our atomic oscillator emits its radiation at a fixed position angle. On the other hand, for $\omega_L/A_{ul} \gg 1$, the radiative rate is extremely small (or the magnetic field extremely strong), and the Larmor precession of the classical oscillator is large relative to the radiative lifetime. The classical atomic oscillator is thus precessing about the magnetic field and emitting radiation at the same time. In this limit it emits evenly at all position angles, and hence the observed polarization will be strongly affected. Figure 1 will be more fully described in § 2.3, but the important result is that the ratio $\omega_L/A_{ul} \propto B/A_{ul}$ essentially determines to what

TABLE 1

DIFFERENCES BETWEEN THE ZEEMAN AND HANLE EFFECTS

Parameter	Zeeman	Hanle
Line processes	Emission or absorption	Resonance-line scattering
Polarization	Circular	Linear
Criterion for applicability	$\Delta v_Z \gg \Delta v_N$[a,b]	$\Delta v_Z \sim \Delta v_N$
Criterion for observability	$\Delta v_Z \gtrsim \Delta v_D$[c]	$\Delta v_Z \lesssim \Delta v_D$
Field sensitivity	$B \gtrsim 1000$ G	1 G $\lesssim B \lesssim$ 1000 G

[a] $\Delta v_Z = g_L \omega_L/2\pi$ is the Zeeman shift.
[b] Δv_N is the natural line width.
[c] Δv_D is the Doppler line width.

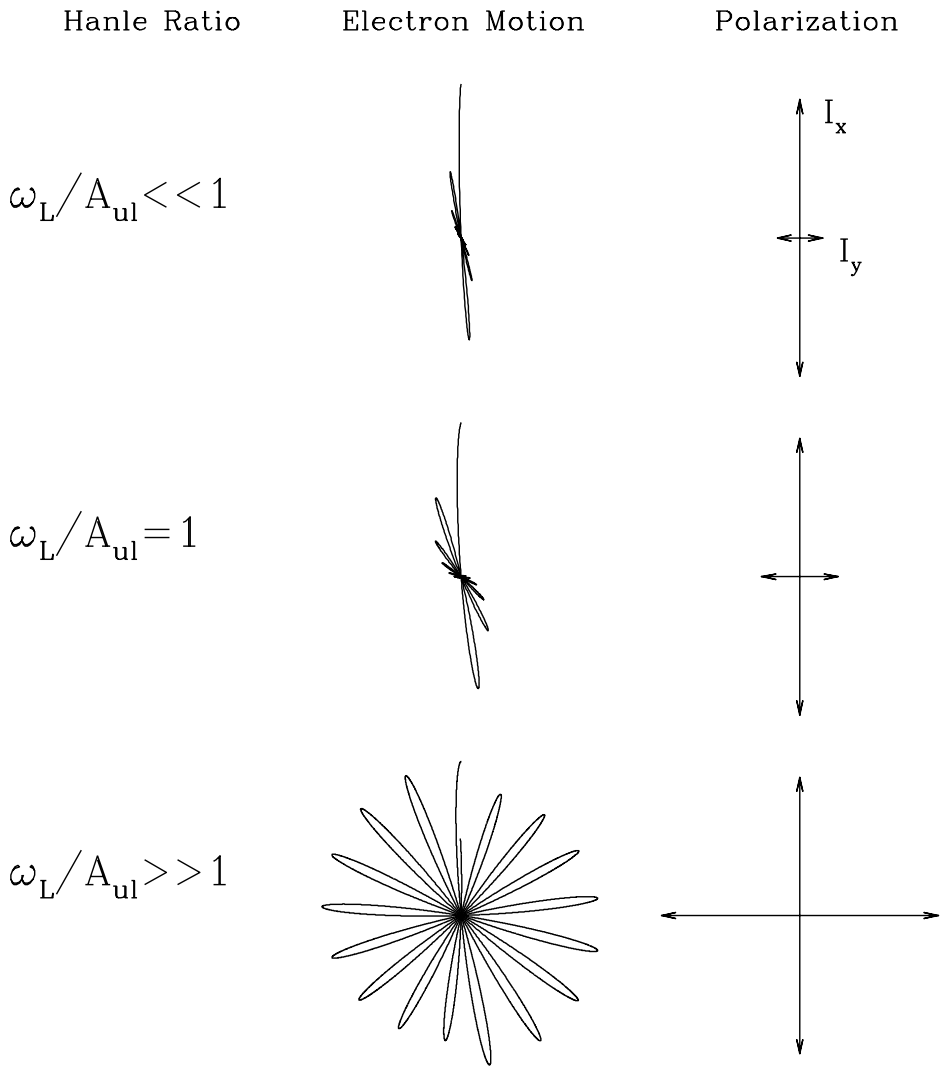

FIG. 1.—The Hanle effect as seen by an observer looking along the magnetic field. Three cases are shown for the ratio of the precession rate ω_L to the radiative rate A_{ul}. The left column gives the ratio ω_L/A_{ul}, the middle column shows the classical electron motion, and the right column schematically indicates the intensities of the scattered light in two orthogonal directions. The cases shown are for the scattering of unpolarized light that is incident from the negative y-direction at the right with the magnetic field on the z-axis and along the viewing line of sight. For weak fields with $\omega_L/A_{ul} \ll 1$, $I_x \gg I_y$, and the scattered light is nearly 100% polarized along the x-direction. For large fields with $\omega_L/A_{ul} \gg 1$, the Hanle precession completes an entire rotation before much damping of the oscillator can occur, so the scattered light is emitted evenly at all position angles (which we call "saturated"), such that $I_x \approx I_y$ and the polarization drops toward zero. The middle row is for $\omega_L/A_{ul} = 1$, which gives the optimal Hanle effect sensitivity to the magnetic field.

degree the magnetic field will alter the polarization of resonance-line scattered light relative to the zero field case.

We should point out that in most astrophysical contexts, it is the Doppler width, Δv_D, that will typically set the threshold at which the individual Zeeman components will emerge from the Doppler smearing. Consequently, the Zeeman effect will not be observable in the presence of Doppler broadening unless

$$\frac{\Delta v_Z}{\Delta v_D} \approx \frac{B}{8960} \frac{\lambda_{ul,3}}{\sqrt{T_4/\bar{m}}} \gtrsim 1 , \tag{2}$$

where B is in gauss, $\lambda_{ul,3}$ is the wavelength of the line transition normalized to 10^3 Å, T_4 is the temperature normalized to 10^4 K, and $\bar{m}$ is the mass in atomic mass units of the ion producing the resonance line. Doppler broadening has two main effects. First, the Doppler broadening causes significant blending of the Zeeman split components. Second, the blending tends to cause cancellation of the polarization in the different Zeeman components. However, in the case of the Hanle effect, the line scattering polarization does *not* suffer cancellation from Doppler broadening. So for UV wavelengths and temperatures typical of hot stars, the Hanle effect is expected to be a viable diagnostic of stellar magnetic field strengths in the subkilogauss range.

2.2. *The Stokes Formulation*

To compute the polarization from extended stellar atmospheres, we adopt the Stokes formalism, in which intensities are treated as 4-vectors. The components of the 4-vector intensity $\boldsymbol{I}_v$ are the familiar Stokes parameters, I, Q, U, and V (Collins 1989). Using these Stokes parameters, the equation of transfer for polarized radiation becomes

$$\frac{d\boldsymbol{I}_v}{d\tau_v} = \boldsymbol{I}_v - \boldsymbol{S}_v , \tag{3}$$

where $\boldsymbol{S}_v$ is the 4-vector source function. The Hanle effect formally enters through the source function, which contains the phase scattering matrix (see eq. [11]). Before discussing

the full source function, let us first consider some of the conditions and approximations appropriate for the problem under consideration.

The atomic data for a specific resonance line are relevant for the Hanle effect through the Hanle angle α_k. From the Appendix, the Hanle angle is defined by the expression

$$\tan \alpha_k = \frac{k g_{\rm L} \omega_{\rm L}}{A_{ul}} = \frac{k g_{\rm L} eB}{2 m_e c A_{ul}} . \quad (4)$$

The quantity $g_{\rm L}$ is the Lánde factor of the upper level and is given by

$$g_{\rm L} = \frac{J(J+1) + L(L+1) - S(S+1)}{2J(J+1)} + g_S \frac{J(J+1) - L(L+1) + S(S+1)}{2J(J+1)} , \quad (5)$$

where $g_S \approx 2$ is the electron spin g-factor, and J, L, and S are the state quantum numbers of the upper level in the standard notation. The quantity k is an integer that can be 0, 1, or 2. There is no Hanle effect for $k = 0$. Only when k is 1 or 2 does the Hanle effect exist. In terms of the classical oscillator, the k-factor arises from the phase relations between the three orthogonal dipole oscillators, that are coupled via the magnetic field. It is these phase relations that govern the polarization properties of the scattered light. Quantum mechanically, the Hanle effect is understood to be an interference effect that occurs when the magnetic sublevels are closely spaced in frequency. In the quantum description, the integer k is the difference of two magnetic quantum numbers in the excited state (Stenflo 1994). For example, in a singlet such as Si III 1207 $3\,^1S_0$–$3\,^1P_1$, the magnetic sublevels of the $^1P_1$ excited state have values $m_j = -1$, 0, $+1$. For all permutations of $m_j - m_j'$, the value of k can be 0, ± 1, ± 2, but only the absolute value of k will matter.

Note that in the definition of the Hanle angle given by equation (4), it has been implicitly assumed that the collisional broadening rate, Γ_C, is small compared to A_{ul}. The effect of collisions is both to depolarize the scattered light and to destroy the quantum interference of the Hanle effect. This occurs because the absorption and emission processes become uncorrelated when collisions are important.

Let us estimate the collisional broadening with a consideration of the frequency of collisions $\Gamma_C \sim n_e \sigma v_e$, where n_e is the electron number density, σ is a collisional cross section (of order the atomic dimension), and v_e is a typical speed of an electron. For the cross section we take $\sigma \sim 10^{-16}$ cm^{-2}; for the particle speed we use the thermal speed for electrons, $v_e \approx (3kT/m_e)^{1/2} \approx 660 (T_4)^{1/2}$ km s^{-1}. Since we are interested in stellar winds, a rough upper limit to the importance of Γ_C can be estimated from the hot dense Wolf-Rayet winds. Assuming a completely ionized pure helium star, the electron number density at the base of the Wolf-Rayet wind is $n_e \sim \dot{M}/8\pi m_{\rm H} R_*^2 v_0$. Using a mass-loss rate for a Wolf-Rayet star of $\dot{M} \sim 3 \times 10^{-5}\ M_\odot$ yr^{-1}, $R_* \sim 2\ R_\odot$, $T_4 \sim 5$, and v_0 equal to the isothermal sound speed, we find that $\Gamma_C \sim 2 \times 10^7$ Hz. Note that an $\dot{M}$ of $10^{-4}\ M_\odot$ yr^{-1} is quite large, even for the Wolf-Rayet stars. Since most strong UV resonance lines have $A_{ul} \gtrsim 10^8$ Hz, collisions will not dominate even for the case of the very strong Wolf-Rayet winds, and especially not for the winds of most other stars, so that $\Gamma_C \ll A_{ul}$ should be a good approximation. This approximation to ignore collisions implies that the frequency redistribution in the wind can be treated as coherent (i.e., undisturbed by collisions).

2.3. *A Dipole Representation of the Hanle Effect*

The classical representation of atomic absorption and reemission of resonance-line photons is extremely useful for understanding the Hanle effect. Recall that a beam of elliptically polarized light may be represented as two orthogonal electric field vectors and that the total beam intensity is proportional to the sum of the squared amplitudes of these electric field vectors (Chandrasekhar 1960). When a beam of such light is scattered by an atom, the induced oscillation of the bound electron can, in general, be decomposed into three orthogonal directions. The distribution of reemitted light will be a superposition of dipolar patterns from the induced orthogonal dipoles. In the presence of a magnetic field, each of the dipoles is caused to precess, according to the $-\boldsymbol{v} \times \boldsymbol{B}$ Lorentz force acting on the electron. Thus, the Hanle effect imposes a coupling between the three dipoles, such that energy can be transferred from one oscillator to the others. With this picture in mind, one can grasp the principle observable effects of resonance-line scattering in a magnetic field for a wide variety of scattering geometries. It is this picture that we intend to develop more quantitatively here.

To determine the dipole strengths, and thus the observed polarization, the Hanle effect phase matrix of the Appendix is used for a geometry in which the magnetic field is aligned with the z-axis. As shown in Figure 2, a beam of unpolarized radiation is incident at the atom in the direction $\cos \theta_i, \phi_i$. Because the incident radiation is unpolarized and the magnetic field is along the z-axis, the scattering polarization depends only on H_{QI} of the Hanle phase matrix, and a consideration of the Hanle effect becomes particularly simple.

The amplitudes of the electric dipoles, $\mathscr{E}_x$, $\mathscr{E}_y$, and $\mathscr{E}_z$, are determined by considering the polarization that would be observed along each of the coordinate axes. For example, an observer on the x-axis will observe scattered radiation produced by the dipoles in the y and z directions, but not from the x dipole since the observer is "looking along" the direction of the atomic oscillation. Using $I_j \propto \mathscr{E}_j$ for the jth coordinate, and H_{QI} from equation (A3) with the adopted geometry (see eq. [17]), the resulting dipole strengths are derived to be

$$2\mathscr{E}_x^2 \approx 1 - \tfrac{1}{4}(1 - 3\cos\theta_i^2) - \tfrac{3}{4}(1 - \cos\theta_i^2)\cos\alpha_2 \cos(2\phi_i + \alpha_2) , \quad (6)$$

$$2\mathscr{E}_y^2 \approx 1 - \tfrac{1}{4}(1 - 3\cos\theta_i^2) + \tfrac{3}{4}(1 - \cos\theta_i^2)\cos\alpha_2 \cos(2\phi_i + \alpha_2) , \quad (7)$$

$$2\mathscr{E}_z^2 \approx \tfrac{3}{2}(1 - \cos\theta_i^2) . \quad (8)$$

Note that the sum $\mathscr{E}_x^2 + \mathscr{E}_y^2 + \mathscr{E}_z^2 = 1$ is a statement of energy conservation for an incident beam of unit intensity. The amplitudes $\mathscr{E}_x$ and $\mathscr{E}_y$ differ only by a minus sign in the last term. This is a reflection of our previous assertion that the magnetic field couples the different dipoles by allowing the energy to be transferred from one mode to another. The gainer and loser of this energy is controlled by the phase, $2\phi_i - \alpha_2$, that depends on the azimuth of the incident light and the magnetic field strength. The amplitude $\mathscr{E}_z$ is not

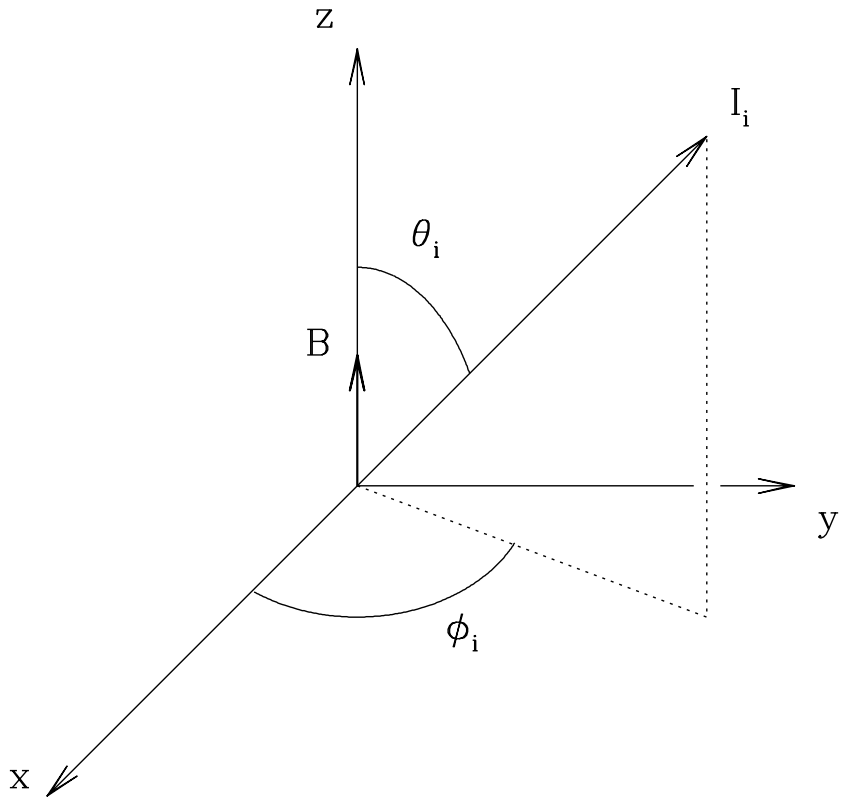

FIG. 2.—The geometry used in the description of the Hanle precession of electric dipoles. Shown is a Cartesian coordinate system with the magnetic field aligned along the z-axis. The intensity $\boldsymbol{I}_i$ is obliquely incident at the origin in the direction cos θ_i, ϕ_i. Radiation scattered by the atom can be represented as that resulting from dipoles along each of the orthogonal axes.

affected by the magnetic field because of our choice of geometry. Since $\mathscr{E}_z \| \boldsymbol{B}$, there is no Hanle precession in this mode because the Lorentz force is zero.

Using expressions (6), (7), and (8) for the dipole amplitudes and a visualization of the Hanle precession from Figure 1, we demonstrate how the Hanle effect may either destroy or create polarization in the scattered beam. Suppose that the unpolarized incident light originates from the negative y-direction, thus cos $\theta_i = 0$ and $\phi_i = \pi/2$. Figure 1 shows the motion of the atomic oscillator as viewed by an observer on the z-axis who is looking along the magnetic field, such that positive x is up and positive y is left. There are three cases of ω_L/A_{ul} shown in Figure 1, as indicated in the left column. The middle column shows the motion of the bound electron as excited by the incident beam of light and precessed by the magnetic field. The rightmost column indicates the observed scattered light in terms of the orthogonal intensities I_x and I_y. Note that we adopt a convention wherein $Q > 0$ for a polarization that is parallel to the z-axis, thus $Q < 0$ is for a polarization perpendicular to the z-axis.

The dipole amplitudes in the x- and y-directions are $\mathscr{E}_x^2 = (1 + \cos^2 \alpha_2)\mathscr{E}_z^2/2$ and $\mathscr{E}_y^2 = (\sin^2 \alpha_2)\mathscr{E}_z^2/2$. In a weak magnetic field, an observer sees radiation that is nearly 100% polarized in the x-direction (see the top row of Fig. 1). As the magnetic field increases, the dipole oscillator in the x-direction is caused to precess about the z-axis, hence a depolarization of the scattered beam is observed, yet the intensity of the light is not diminished. As the field strength increases to large values, the depolarization becomes nearly complete for $\omega_L \gg A_{ul}$ (see the bottom row of Fig. 1). In this case the depolarization is said to be "saturated," because larger magnetic fields can produce no discernible change in the observed polarization. The saturated case is still of interest, for it indicates the presence of a magnetic field and a lower limit to the field strength can be estimated. An accurate determination of the field strength is best made in the case $\omega_L \approx A_{ul}$ (see the middle row of Fig. 1), for which the depolarization is significant but not complete.

In addition to a reduction of the polarization, the orientation of the polarization is no longer the x-axis. The position angle of the polarization is $\frac{1}{2} \tan^{-1} \mathscr{E}_y/\mathscr{E}_x$, as measured from the x-axis. This description is true only for an observer along the z-axis. In the right-hand column of Figure 1, notice the strengthening of the scattered intensity in the y-direction as the field strength is made to increase. Its appearance, because of the Hanle effect, will cause rather different changes in the polarization for observing lines of sight other than along the z-axis.

For example, consider an observer located on the positive x-axis (i.e., perpendicular to both the magnetic field and the direction of the incident intensity). The dipole amplitudes along the z and y-axes are $\mathscr{E}_z^2 = 3/2$ and $\mathscr{E}_y^2 = (\sin^2 \alpha_2)\mathscr{E}_z^2/2$. The scattered light is completely polarized in the z-direction when there is no magnetic field; however, the Hanle effect results in a depolarization with an increase in total intensity. Alternatively, for an observer along the y-axis, the dipole amplitudes of interest are $\mathscr{E}_z^2 = 3/2$ and $\mathscr{E}_x^2 = (1 + \cos^2 \alpha_2)\mathscr{E}_z^2/2$. Since the unpolarized incident beam is forward scattered, the scattered light will likewise be unpolarized in the zero field case. But as a magnetic field is applied in the z-direction, the intensity of the scattered

light is decreased and the light becomes *increasingly polarized* along the z-direction. Note that in these two cases, the decrease or increase in polarization for observers along the x- or y-axes, respectively, is never so great as to produce complete polarization or depolarization, even as the magnetic field strength is increased to large values.

The effective dipole representation of the Hanle effect is conceptually useful, although quantitatively limited. We have illustrated how the Hanle effect may destroy or create polarization and alter the orientation of the net polarization, and how these effects depend on the observer's perspective, the magnetic field orientation, and the direction of incident light. The most useful aspect of the dipole representation is the explicit portrayal of the Hanle effect as a consequence of precession. Dipoles that are parallel to the magnetic field suffer no Hanle effect; only dipole components perpendicular to the field are precessed. This description is particularly useful in the strong field limit (i.e., $\alpha_2 \rightarrow \pi/2$), for which the Hanle precession completes many revolutions, leading to rather straightforward predictions. When dealing with more complicated geometries, such as circular rings or quadrupolar magnetic fields, the dipole picture permits a qualitative understanding of the results.

3. INTEGRATED LINE PROFILES FROM AXISYMMETRIC ENVELOPES

Here theoretical line polarizations from axisymmetric circumstellar envelopes are derived for a sequence of elementary density distributions. In this paper, results are derived for the polarization as integrated over the full line profile. In a subsequent paper, a discussion of the Hanle effect for the shape of the polarized line profile will be presented.

3.1. *The Scattering Geometry*

Referring to Figure 3, we construct a coordinate system in which the Cartesian coordinates (X, Y, Z) refer to those of the observer and (X_*, Y_*, Z_*) refer to those of the star. The Z_*-axis is the symmetry axis of the star. We take the Y- and Y_*-axes to be coincident (not shown); hence, X, X_*, Z, and Z_* all lie in the same plane. In this system the observer views the star from the Z-axis, and the line-of-sight inclination angle of the stellar system, i, is defined as the angle between the Z and Z_*. Hence, $i = 0$ means that the observer sees the star pole-on, and $i = \pi/2$ refers to an edge-on viewing line of sight. Figure 3 shows a vector $\boldsymbol{r}$ from the stellar origin to a point P, with spherical coordinates (r, ϑ, φ) as measured in the star system. Cylindrical coordinates of point P are (ρ, φ, Z_*). Originating at the point P are two unit vectors, $\boldsymbol{n}_i$ and $\boldsymbol{n}_s$, that represent the directions of incident and scattered intensities, respectively. The subscripts i and s shall hereafter be used to denote properties of the incident and scattered light. Finally, the unit vector $\boldsymbol{n}_B$ indicates the direction of the magnetic field B at the point P.

For deriving the polarization that results from scattering, only the directions of the radiation field and magnetic field at the *location* of the scatterer (i.e., point P) must be known.

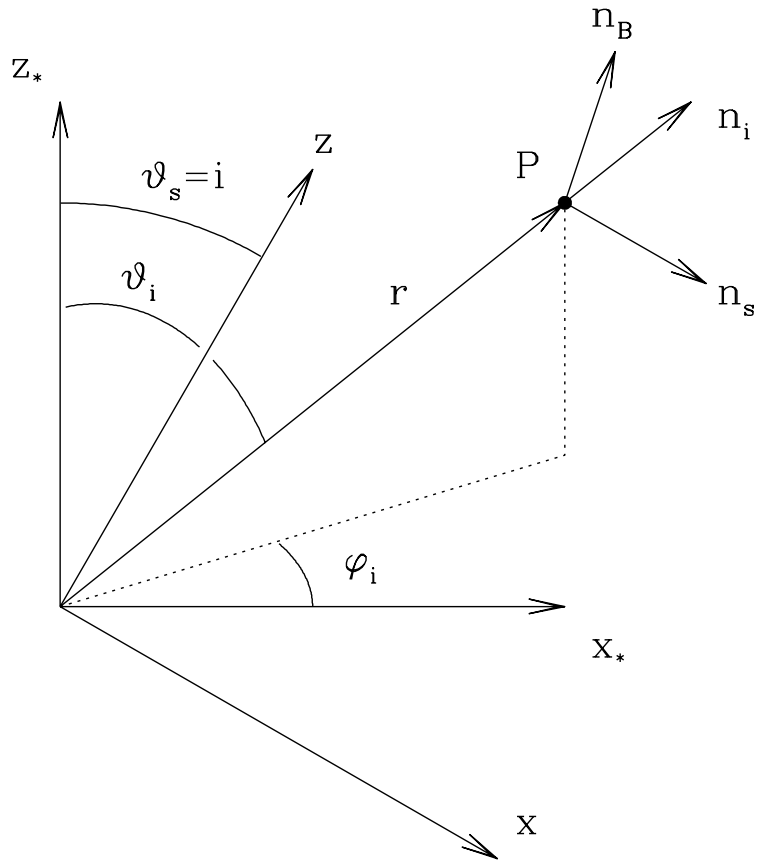

FIG. 3.—The stellar coordinate system. The Z_*-axis is the symmetry axis, and the observer views the star along the Z-axis that is located in the X_*-Z_* plane. The Y and Y_*-axes (not shown) are into the page and coincident. The viewing inclination angle, i, is measured from the Z_*-axis to the Z-axis. The angles ϑ and φ are the spherical polar angles in the stellar coordinate system. The three arrows labeled $\boldsymbol{n}_B$, $\boldsymbol{n}_i$, and $\boldsymbol{n}_s$ are unit vectors for the directions of the magnetic field, incident intensity, and scattered intensity, respectively. The vector $\boldsymbol{r}$ is the spatial position of the scattering point P with respect to the origin.

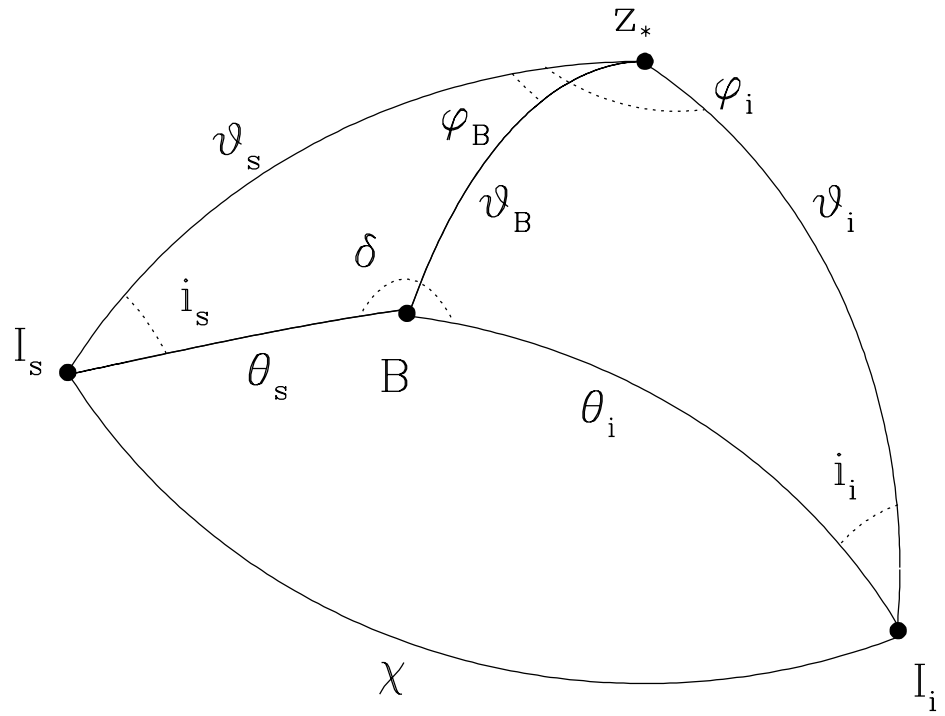

FIG. 4.—The scattering geometry. This figure shows the scattering geometry at the scatterer (i.e., point P of Fig. 3). The angles ϑ and φ are the spherical polar angles in the stellar coordinate system. The angles θ and δ are in the coordinate system for which the magnetic field direction is the *local* z-axis. The angles i_i and i_s are the Mueller rotation angles used to rotate the Stokes vectors to and from the local coordinates of the magnetic field to those of the observer's measurement axes. The subscripts i, s, and B refer to the incident radiation, the scattered radiation, and the magnetic field, respectively. The scattered intensity $\boldsymbol{I}_s$ is parallel to the observer's Z-axis. Finally, χ is the angle between the incident and scattered intensity rays.

Thus, Figure 4 shows the scattering geometry as centered on the scattering particle, with point P now located at the origin. The new geometric quantities appearing in this figure are as follows:

1. ϑ_i is the angle between the Z_*-axis and the incident intensity.
2. ϑ_s is the angle between the Z_*-axis and the scattered intensity.
3. θ_i is the angle between the magnetic field at P and the incident intensity.
4. θ_s is the angle between the magnetic field at P and the scattered intensity.
5. δ is the azimuthal angle $(\phi_s - \phi_i)$ between I_i and $\boldsymbol{I}_s$ as measured around $\boldsymbol{B}$.
6. ϑ_B is the angle between the Z_*-axis and the magnetic field.
7. i_i is the Mueller rotation angle for the incident intensity.
8. i_s is the Mueller rotation angle for the scattered intensity.

Note that ϑ_s is equal to the viewing inclination angle, i. The application of the Mueller rotation matrix (see the Appendix) insures that the polarimetric properties of the scattered light (i.e., the Stokes parameters) arising from different regions in the scattering envelope are consistently projected onto the observer's axes for measuring Q and U. The other angular quantities are necessary because the scattering phase matrix is determined by the scattering geometry in a coordinate system where the magnetic field is along the *local* z-axis (Stenflo 1994). In general, a reduction of the spherical trigonometry is quite daunting unless the magnetic field geometry is particularly simple, examples of which are considered in § 3.3.

3.2. *The Optically Thin Assumption*

In an optically thin medium, the radiation transfer simplifies immensely. There is no attenuation of light by the stellar envelope, neither between the stellar source and the scatterer nor between the scatterer and the observer, so every photon that is scattered in the stellar envelope will also emerge from it. Normally, the consequences of backscattering of photons into the stellar atmosphere and occultation of scattering material on the far side of the star should be included. In this paper we ignore the complications of backscattering and occultation and consider only the case of a purely radial radiation, such as would be expected from a point star.

For distant stars it is the flux of line emission that observers can measure, so to calculate the polarized line emission from a stellar wind, we employ the Sobolev theory of radiation transfer in a moving medium. In the Sobolev theory, penetration and escape probabilities are used to model the radiative transfer through the wind. As implied by their names, the penetration probability governs the degree to which direct stellar light can reach a given point in the flow, and the escape probability determines the likelihood that a photon scattered at a given point will emerge from the circumstellar envelope without further interaction with the wind material. A derivation of Sobolev theory will not be given here, but the reader is referred to Mihalas (1978) and Lamers & Cassinelli (1996) and references therein for more detailed discussions.

In Sobolev theory the important parameter that determines whether the line at a given frequency will be optically thin or thick is the Sobolev optical depth, given by

$$\tau_{\rm Sob} = \int \sigma_l \, n\delta(\Delta v) ds \ , \tag{9}$$

where σ_l is the frequency integrated cross section, n is the number density of the scattering atoms, and the δ-function causes the optical depth to be zero along the line of sight until the point where the Doppler shift from line center, due to the bulk motion of the wind material, is equal to Δv. Hence, Δv is a function of the line-of-sight path length s through the wind. The atomic cross section is given by $\sigma_l = \lambda_{ul}^2 g_u A_{ul}/8\pi g_l$, where g_u and g_l are the statistical weights for the upper and lower levels. A consideration of the penetration and escape probabilities reveals that the line at a given frequency will be optically thin when the Sobolev optical depth $\tau_{\rm Sob} \lesssim 1$.

With an expression for the line optical depth, we can now predict the observable polarized flux of the line. Assuming that the line is optically thin, the observed intensity is given by $\boldsymbol{I}_{v,s} \approx \boldsymbol{S}_v \tau_{\rm Sob}$, where $\boldsymbol{S}_v$ is the source function. The total Stokes flux of resonance-line scattered photons is given by the following integral over the scattering volume:

$$\boldsymbol{F}_s = \int \mu \boldsymbol{I}_{v,s} \, dv \, d\Omega = \frac{1}{d^2} \int \boldsymbol{S}_v \, \sigma_l \, n\delta(\Delta v) dv \, dV \ . \tag{10}$$

The first integral of equation (10) gives the standard definition for the observed flux in emission, where $d\Omega = dA/d^2$ is the differential solid angle, dA is the differential area element transverse to the line of sight, and d is the distance to the star. As the distance to the star is much larger than the size of the envelope, $\mu \approx 1$. The second integral of equation (10) results from substituting for $\tau_{\rm Sob}$ using equation (9) and defining the differential volume element dV as the product $dA\,ds$. Because the star is treated as a point-source, absorption of the stellar continuum by the circumstellar envelope is neglected.

To complete the derivation of the flux, the source function is required. The source function is given by

$$\boldsymbol{S}_v = \frac{1}{4\pi} \int L(i_s) H(\boldsymbol{n}_i, \boldsymbol{n}_s) L(i_i) \boldsymbol{I}_{v,i} \, d\Omega \ , \tag{11}$$

where $L(\gamma)$ is the 4×4 Mueller rotation matrix through an angle γ, H is the 4×4 Hanle scattering phase matrix, and $\boldsymbol{I}_{v,i}$ is the incident intensity. Assuming a point-source star that emits unpolarized light only, the incident Stokes intensity is $\boldsymbol{I}_{v,i} = (k_0 \, I_*, 0, 0, 0)\delta(\Omega - \Omega_0)$, where I_* is the intensity at the stellar surface and Ω_0 is the solid angle in the direction of the atomic scatterer. The quantity k_0 is determined by requiring the flux in the radial direction to be $\mathscr{F}_v = L_v/4\pi r^2$; hence, it can be shown that $k_0 = \mathscr{F}_v/I_*$. The assumption of unpolarized stellar light yields a tremendous reduction of the source function, because the only nonvanishing element of $\boldsymbol{I}_{v,i}$ is the intensity. As a consequence, the product $H(\boldsymbol{n}_i, \boldsymbol{n}_s)L(i_i)\boldsymbol{I}_{v,i}$ simplifies to $\mathscr{F}_v(r)(H_{II}, H_{QI}, H_{UI}, 0)\delta(\Omega - \Omega_0)$, and the source function becomes

$$\boldsymbol{S}_v = \frac{\mathscr{F}_v(r)}{4\pi} L(i_s) \begin{Bmatrix} H_{II} \\ H_{QI} \\ H_{UI} \\ 0 \end{Bmatrix} , \tag{12}$$

where H_{II}, H_{QI}, and H_{UI} are computed from expressions found in the Appendix.

In writing expressions (10) and (12), we have tacitly assumed complete frequency redistribution. Stenflo (1994) considers the general frequency redistribution for the line scattering with magnetic fields. In the line wings, far from line center v_0 such that $\Delta v \gg \Delta v_{\rm D}$ and $\Delta v \gg \Delta v_{\rm Z}$, the scattering is both frequency coherent and independent of the magnetic field, so there is no Hanle effect. The frequency coherence results because the frequency shift required for a photon absorbed in the line wings to appear in the line core is so large that its probability of occurring (assuming a Maxwellian distribution of velocities) is negligibly small. The Hanle effect vanishes in the line wings because the time spent by a given electron in the line wings tends to be shorter than at line center. This is a reflection of the fact that the Lorentzian broadening is a probability distribution for the electron state. The Lorentzian wings represent improbable states for the electron energy, hence an electron that happens to be at those frequencies will not remain there long, the duration being proportional to $(v - v_0)^{-1}$, so there will be little time for Hanle precession to be significant (Omont, Smith, & Cooper 1973).

For the line core and weak magnetic fields (i.e., $\Delta v \lesssim 3\,\Delta v_{\rm D}$ and $\Delta v_{\rm Z} \ll \Delta v_{\rm D}$), the Zeeman splitting is much smaller than the Doppler width, and the Doppler broadening yields a frequency averaging of the redistribution matrix. In the line core, this frequency averaging permits a separation of the frequency dependence from the polarimetric properties of the scattered light. Thus, equation (12) is valid for the line core, assuming complete frequency redistribution.

Using equations (10), (12), (A1), (A2), and (A6), the observed Stokes flux from the envelope is

$$\boldsymbol{F}_s = \frac{\sigma_l L_v}{16\pi^2 d^2} \int n(r, \mu_i) \times \begin{pmatrix} H_{II} \\ H_{QI} \cos 2i_s + H_{UI} \sin 2i_s \\ -H_{QI} \sin 2i_s + H_{UI} \cos 2i_s \\ 0 \end{pmatrix} dr \, d\mu_i \, d\varphi_i \ , \tag{13}$$

where we have taken for the differential volume element $dV = dV_* = r^2 dr \sin \vartheta_i \, d\vartheta_i \, d\varphi_i = r^2 dr \, d\mu_i \, d\varphi_i$. The integral is most naturally performed in the stellar coordinates versus the observer's, because it is in the stellar coordinates that the envelope density and magnetic field distributions are most easily expressed. The phase matrix elements H_{II}, H_{QI}, and H_{UI} and the Mueller angle i_s are all functions of the stellar coordinates. In equation (13), we have also evaluated the frequency integral, assuming that the continuum is flat over the frequencies of the line; thus, $\int L_v \sigma_l \delta(\Delta v) dv \approx L_v(\lambda_{ul})\sigma_l$.

We make one further simplification by virtue of our choice of coordinate system. Although arbitrary line-of-sight viewing inclinations are allowed, the X_*-Z_* plane has been chosen coincident with the X-Z plane of the observer, so that the total Stokes U-flux as integrated over the entire scattering volume vanishes by symmetry. So for an integrated line profile, the net polarization results from the Q-flux alone. Assuming that the total scattered flux is negligible relative to the direct stellar light (so that $F_s^I \ll \Delta v_{\rm L} \, L_v/4\pi d^2$, with $\Delta v_{\rm L} = 2v_\infty/\lambda_{ul}$ being the wind broadened line width), we define the percent polarization of the

envelope as

$$p \approx \frac{F_s^Q}{\Delta v_L L_v/4\pi d^2} = \frac{1}{4\pi}\tau_l \int \tilde{n}(x, \mu_i) \times (H_{QI} \cos 2i_s + H_{UI} \sin 2i_s) dx\, d\mu_i\, d\varphi_i\,, \quad (14)$$

where $x = r/R_*$ is the normalized radius, $\tilde{n} = n/n_0$ is the normalized number density for an axisymmetric wind, and n_0 is the density normalization constant. The parameter n_0 is not of direct concern in this discussion but will be defined later in § 4.2. Note that the integral of equation (14) is over the volume that contains the scatterers, so x ranges from 1 to ∞. The occurrence of the Hanle effect is confined to the integral part of equation (14) only; τ_l is a constant scaling factor that is related to basic parameters of the star and the wind.

If the integral part of equation (14) is considered as a response of the envelope density and magnetic field distributions to the polarizing effects of resonance-line scattering, then the constant τ_l may be taken as the polarization signal amplitude. The symbol τ_l is chosen for this constant because of its similarity in form to that of an optical depth. The value of this parameter is implicitly derived from a consideration of the frequency mean line optical depth:

$$\bar{\tau}_{\rm Sob} = \frac{1}{\Delta v_L}\int \tau_{\rm Sob}\, dv = \frac{\sigma_l n_0 R_*}{2v_\infty/\lambda_{ul}} \int \tilde{n}\, dx \equiv \tau_l \int \tilde{n}\, dx\,. \quad (15)$$

From equation (15), $\tau_l = \lambda_{ul}\sigma_l R_* n_0/2v_\infty$ and represents the average optical depth in the line. The value of τ_l is especially important because of its relation to the line optical depth. Our derivation for the line polarization of equation (14) requires that the line be optically thin at each point in the profile. If $\tau_{\rm Sob} \lesssim 1$ at each frequency in the line, then the frequency mean optical depth $\bar{\tau}_{\rm Sob}$ must be $\lesssim 1$, and τ_l is also expected to be $\lesssim 1$. We will discuss τ_l further in § 4.2 in the context of selecting stellar targets and lines for observations, for which our theoretical results, derived next, will be applicable.

3.3. *Results for Axisymmetric Rings*

As we are concerned with axisymmetric geometries, it is first useful to develop results for circular rings, as was done by Brown & McLean (1977), that can be used as the building blocks for more interesting configurations. Analytic results are presented for the scattering of light by a thin axisymmetric ring located at colatitude ϑ with a cylindrical radius of $r \sin \vartheta$, as measured from the stellar axis.

From equation (14), the net polarization from a ring is

$$p_{\rm ring} = \frac{1}{4\pi}\tau_l\, \tilde{n}(x, \mu_i) \int_0^{2\pi} (H_{QI} \cos 2i_s + H_{UI} \sin 2i_s) d\varphi_i\,. \quad (16)$$

Even with the assumptions of an unpolarized stellar point source and an optically thin medium, the solution to $p_{\rm ring}$ remains nontrivial, because of the complicated angular dependencies of the Hanle phase matrix elements H_{QI} and H_{UI}. The main difficulty is that the Hanle phase matrix is formulated for a coordinate system defined by the magnetic field. For this reason, analytic solutions remain elusive, existing for only a handful of simplified magnetic geometries, including radial, B_r, meridional, B_ϑ, toroidal, B_φ, cylindrical radial, B_ρ, and axial, B_Z, fields. These five field distributions are special, because in each case the magnetic field is aligned with a natural coordinate direction associated with the stellar system. As a consequence, major simplifications result. We choose to concentrate on these few semianalytic cases to demonstrate the diverse polarimetric behavior that can result with the Hanle effect.

It is a general property of the Hanle effect that the scattering is unaffected by the magnetic field if the incident intensity distribution is axially symmetric about the magnetic field direction; thus, the Hanle effect vanishes in such cases, leaving only the normal resonance-line scattering. Such is the case for a radial magnetic field, because of the collinearity of the field direction and incident radiation. This result is readily explained by our electric dipole model: for a radial magnetic field, the two orthogonal dipoles that are excited by the incident radiation will precess about the magnetic field by equal amounts. Thus, resonance-line scattering in an optically thin stellar envelope with a radial magnetic field yields no Hanle effect.

The case of an axial field is the next simplest to consider, because the magnetic field is already aligned with the stellar symmetry axis. In this case there are two major simplifications: (1) the Mueller matrix angle i_s equals 0, and (2) the Hanle effect scattering angles reduce to the stellar coordinates, giving $\theta_s = \vartheta_s = i$, $\theta_i = \vartheta_i$, $\phi_s = \varphi_s = 0$, and $\delta = -\varphi_i = -\phi_i$. The geometric simplifications are so great that we present the scattered Stokes flux per unit solid angle in its entirety. The amount of flux scattered into the observer's line of sight by a small ring segment of differential solid angle $d\Omega_i$ is

$$\frac{d\boldsymbol{F}_s(B_Z)}{d\Omega_i} = \frac{3E_1\tau_l L_v\, dx}{512\pi^2 d^2} \times \begin{bmatrix} \dfrac{8}{3E_1} + \dfrac{1}{3}(1 - 3\cos^2 i)(1 - 3\cos^2 \vartheta_i) + 2a(-\varphi_i) \\ \qquad \times \sin 2i \sin 2\vartheta_i + c(-\varphi_i)\sin^2 i \sin^2 \vartheta_i \\ \sin^2 i\,(1 - 3\cos^2 \vartheta_i) - 2a(-\varphi_i)\sin 2i \sin 2\vartheta_i \\ \qquad -c(-\varphi_i)(1 + \cos^2 i)\sin^2 \vartheta_i \\ -b(-\varphi_i)\sin i \sin 2\vartheta_i - 2d(-\varphi_i)\cos i \sin^2 \vartheta_i \\ 0 \end{bmatrix}. \quad (17)$$

The magnetic effects enter exclusively through the functions $a(-\varphi_i)$, $b(-\varphi_i)$, $c(-\varphi_i)$, and $d(-\varphi_i)$ that are defined in equation (A4) of the Appendix.

To obtain $p_{\rm ring}$, an integration of equation (17) is required. Of course, the net U-flux is zero, but interestingly, the Hanle effect for both Stokes I and Q parameters also vanishes upon integration, so that the total scattered flux from a ring with the axial field is the same that would be found without the axial magnetic field. A corollary is that there is no Hanle effect for an axisymmetric envelope with axial magnetic fields. There is, however, a Hanle effect at each individual point along the ring perimeter, so an extended stellar envelope in bulk motion with an axial field should show a Hanle effect along the polarized line profile (Ignace, Cassinelli, & Nordsieck 1997).

For the remaining three simple field distributions, B_ϑ, B_φ, and B_ρ, the polarization from a ring segment is still a cumbersome function of the geometry, even though the magnetic field is conveniently aligned with a coordinate axis. However, several terms in the expression for the polariza-

tion from a ring segment are odd functions of azimuth and integrate to zero, so that the net polarization from the ring as a whole simplifies immensely. After some simplifications, the net ring polarizations for these magnetic field geometries were solved by numerically integrating the polarized flux per unit azimuth around the ring perimeter to obtain $p_{\rm ring}$.

A summary of the results for each of the five special magnetic field distributions are listed in Table 2. The first column indicates the type of magnetic field, and the second gives $p_{\rm ring}$ expected for each case. Note that the expressions in Table 2 have been normalized by $3\tau_l E_1/16$. The first row of Table 2 gives the result for the nonmagnetic case, which is simply that of Brown & McLean (1977). The polarization for each of these analytic cases is proportional to $\sin^2 i$, which lends confidence to our numerical investigations that reveal that the $\sin^2 i$ dependence likely exists for arbitrary field strengths and geometries. Further note that there is a transition latitude, ϑ_t, at which the polarization goes to zero independent of the viewing inclination. In the absence of a magnetic field, ϑ_t is just the van Vleck angle. The van Vleck angle is the latitude at which the solid angles of the two polar caps equal that of the equatorial band. The presence of a magnetic field causes ϑ_t to differ from 54°.7. Using Table 2, we discuss ϑ_t for the cases of B_ϑ, B_φ, and B_ρ.

For meridional and cylindrical radial magnetic fields, the ring polarization is modified by the Hanle effect in the same way. In both cases the effect of a magnetic field is to increase the polarization toward larger positive values. To show this, consider the transition colatitude at which $p_{\rm ring} = 0$. The transition colatitude when either B_ϑ or B_ρ is present becomes $\vartheta_t = \cos^{-1}[2/3(1 + \cos^2 \alpha_2)]^{1/2}$. It ranges from 54°.7 for zero magnetic field, moves poleward as the field increases, and attains a maximum colatitude of 35°.3 at large field strengths. The polarization of a ring poleward of 54°.7 would normally be negative (i.e., polarized transverse to the symmetry axis), but the Hanle effect makes the ring less negatively polarized. If the field is large enough and if the ring is located at latitudes between about 35° and 55°, then the Hanle effect can actually cause a 90° position angle flip so as to align the net polarization of the ring *with* the symmetry axis.

The result for a toroidal field differs significantly from the previous cases. First, the line polarization is a somewhat more complicated function of geometry and the Hanle angle α_2, with the result that there is a finite field strength at which the polarization of an equatorial ring becomes negative. This condition is met when $\cos^2 \alpha_2 < \frac{1}{3}$ (i.e., α_2 is greater than the van Vleck angle), corresponding to $B_\varphi > 2^{1/2} m_e c A_{ul}/g_u e$. We also note that $p_{\rm ring}(B_\varphi)$ contains the term $\sin 2\vartheta$, which is an odd function of latitude; hence, the net polarization from the upper hemisphere will differ from that of the lower, *even* if the density distribution is top-bottom symmetric.

TABLE 2

ANALYTIC EXPRESSIONS FOR THE HANLE EFFECT IN AXISYMMETRIC RINGS

Field Type	Integrated Line Polarization
$B = 0$.....	$\sin^2 i\,(1 - 3\cos^2 \vartheta)$
B_r.....	$\sin^2 i\,(1 - 3\cos^2 \vartheta)$
B_Z	$\sin^2 i\,(1 - 3\cos^2 \vartheta)$
B_ρ	$\sin^2 i\,[1 - \frac{3}{2}\cos^2 \vartheta\,(1 + \cos^2 \alpha_2)]$
B_ϑ	$\sin^2 i\,[1 - \frac{3}{2}\cos^2 \vartheta\,(1 + \cos^2 \alpha_2)]$
B_φ	$\sin^2 i\,(\frac{3}{4}\sin 2\alpha_2 \sin 2\vartheta - \frac{3}{2}\cos^2 \alpha_2 \cos 2\vartheta - \frac{1}{2})$

In summary, all five of the simple field distributions that we have considered indicate that (1) $p_{\rm ring}$ has a $\sin^2 i$ dependence and (2) the extent to which the Hanle effect is seen depends on the magnetic field geometry. For field geometries that are symmetrically oriented to the radiation field, there will be no Hanle effect. In other cases the field geometry can lead to a decrease or an increase of the polarization. Even sign changes in the polarization (i.e., position angle flips) can result under certain conditions. Later, we will show that some of the ambiguities can be removed through multiline observations. The next task is to employ the results for rings to the more physical case of extended envelopes.

3.4. *Results for Extended Envelopes*

Given a solution for a thin ring, the Hanle effect for an extended envelope can be found by summing up the ring contributions over the volume of interest, which is an integral over radius and latitude:

$$p_{\rm env} = \int_V p_{\rm ring}(x, \mu_i)dx\,d\mu_i\ . \tag{18}$$

Perhaps the most significant types of axisymmetric geometries to consider for stellar envelopes are disks, plumes, and shells. For this reason we consider the Hanle effect for the more general case of volumes that are sectors of revolution, with the spherical case treated separately.

3.4.1. *The Hanle Effect for Sectors of Revolution*

To derive the Hanle effect for a sector of revolution (henceforth referred to as just "sector"), we first consider a conical sheet. For a general conical surface with negligible angular extent and an opening angle of ϑ_i, the polarized flux is

$$p_{\rm cone}(\mu_i) = \int_1^\infty p_{\rm ring}(x, \mu_i)dx\ . \tag{19}$$

Equation (19) is a radial integration that involves the number density and the radial dependence of the magnetic field. Note that $p_{\rm cone}$ applies to a cone in only one hemisphere.

Conceptually, a sector is then a sequence of adjacent conical sheets. Thus, to determine the polarization of a sector volume, equation (19) is integrated over the latitudes of interest, yielding

$$p_{\rm sec} = \int_{\mu_1}^{\mu_2} p_{\rm cone}(\mu_i)d\mu_i\ , \tag{20}$$

where $\mu_1 = \cos \vartheta_1$ and $\mu_2 = \cos \vartheta_2$ denote the lower and upper latitudinal boundaries of the sector, respectively. The sector is said to be a polar plume if $\mu_2 = 1$, in which case the scattering material is confined to latitudes poleward of ϑ_1. On the other hand, if $\mu_1 = 0$, then the sector is the upper half of an equatorial disk with scatterers located between ϑ_2 and $\pi/2$.

Let us now consider an actual computation of equations (19) and (20). Before, when we determined $p_{\rm ring}$, both the number density and the magnetic field distribution were constant at every point on the ring, because of the assumption of axisymmetry. Now, however, these distributions

must be specified to calculate the envelope polarization. For simplicity, we initially assume that the number density and magnetic field distribution are functions of radius only. We chose the normalized number density to be a power law in radius, with $\tilde{n}(x) = x^{-(2+t)}$, where n_0 has been defined in equation (30). Note that the $t = 0$ case is analogous to a piecewise spherical stellar wind expanding at constant radial velocity. We also assume a power law magnetic field distribution with $B = B_* x^{-m}$, where B_* is the magnetic field strength at the stellar surface.

Figure 5 shows the normalized line-integrated polarization plotted as a function of $\tan \alpha_2(R_*) = B_*/B_{\rm Hanle}$. The parameter $B_{\rm Hanle} = m_e c A_{ul}/e g_{\rm L}$ and represents the magnetic field strength at which $\omega_{\rm L}$ approximately equals A_{ul}. The normalization of the line polarization includes the $\sin^2 i$ factor, so the curves of Figure 5 are valid for all viewing perspectives and may be considered as the maximum polarization obtainable for a given stellar envelope if viewed edge-on.

Four different sector geometries are considered in the figure: a thick disk, a thin disk, a broad polar plume, and a narrow polar plume. Note that the sector geometry for all four cases is symmetric about the equator (e.g., there are plumes extending from the star in both hemispheres). In each case the polarizations are computed using $t = 0$ and $m = -1$ in the power-law distributions of the density and magnetic field. The half-opening angles, $\Delta\vartheta$, have been chosen so that the solid angle of the narrow plume is roughly that of the thin disk, and similarly for the broad plume and thick disk. For the broad plume and thick disk, $\Delta\vartheta$ is chosen so that the van Vleck latitude is a boundary of the respective sectors; thus, in the absence of a magnetic field, the polarizations for these two geometries are maximized and equal in magnitude but opposite in sign.

For each sector geometry, Figure 5 shows three curves for the polarization. The horizontal line in each case is the resonance-line polarization expected in the absence of a magnetic field. The other two cases are for meridional and toroidal fields, as indicated. Recall that radial and axial field configurations yield no Hanle effect for the integrated line polarization, and a cylindrical radial field gives the same result as a meridional field. The polarization varies most

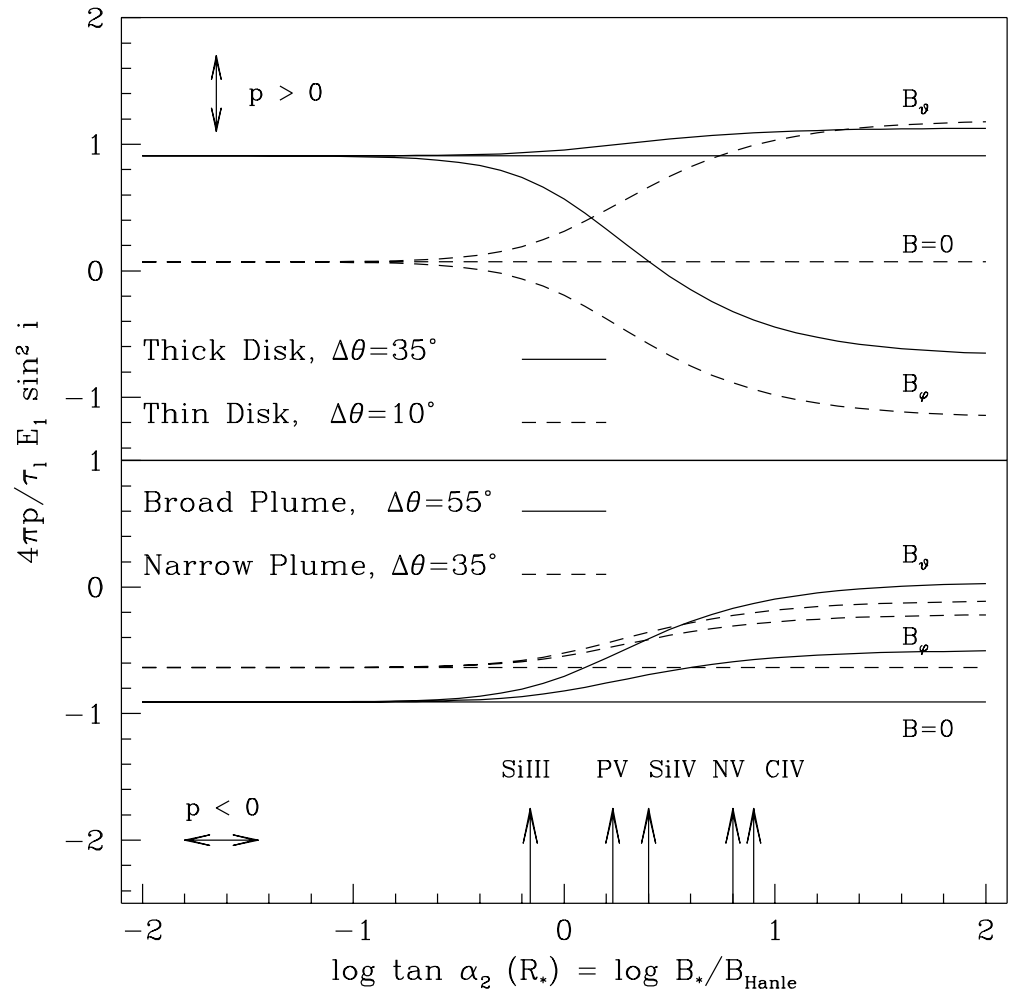

FIG. 5.—Integrated line polarizations. The top panel is for polar plumes and the lower for equatorial disks. The vertical axis is the normalized integrated line polarization; the horizontal axis is $\tan \alpha_2(R_*) = B_*/B_{\rm Hanle} \sim B_*/A_{ul}$ (see eq. [4]). Two different half-opening angles, $\Delta\vartheta$, are considered for both plumes and disks, as indicated by the line types. There are three curves for each geometry, representing different magnetic field configurations ($B_* = 0$, B_ϑ, and B_φ), as indicated. At the bottom is shown an ensemble of line distributions. For a surface magnetic field of 100 G, each arrow indicates where a line measurement for a given atomic species would be placed along the abscissa. Changing the surface field strength does not change the relative positions of the arrows but shifts the line ensemble as a whole to the left or right. For a real star, the measured polarizations for the line ensemble are allowed to slide horizontally until a best fit is obtained to one of the diagnostic curves, at which point both the field geometry and the surface field strength are determined. Note that for the curves shown here, the magnetic field is assumed to decrease as $B \sim r^{-1}$ in each case.

rapidly with tan α_2 between values of about $\frac{1}{4}$ to 10; outside of this range the polarization tends toward asymptotic values. Also shown at the bottom of Figure 5 is an ensemble of vertical arrows labeled by ions commonly observed in the winds of many hot stars. These can be ignored for the present but will be discussed later in § 4 in terms of diagnosing stellar magnetic fields from polarimetric measurements using these theoretical curves.

The results shown in Figure 5 for disk and plume geometries indicates that the Hanle effect can have major consequences for the resonance-line scattered polarization, and that the variation of the line polarization relative to the zero field case is greatest at large values of $B_*/B_{\rm Hanle}$ (i.e., in the saturated limit). The polarization is seen to increase in some cases and decrease in others. It may also change sign, as in some cases when $B = B_\varphi$. As indicated in the figure, a change of sign in the polarization implies a position angle flip of 90°. In the next section, the somewhat simpler spherical geometry for the density distribution is considered, and results are described using more complicated magnetic geometries.

3.4.2. *The Hanle Effect for Spherical Envelopes*

In the zero field case, an unresolved spherical shell will yield net zero polarization, because the polarized flux is axially symmetric about the line of sight. However, a magnetic field can break this symmetry even if the density distribution is spherically symmetric. To derive the polarization from a spherically symmetric envelope, we first consider geometrically thin spherical shells, analogous to our construction of sectors from conical surfaces.

For a spherical shell, the observed polarization is

$$p_{\rm shell}(x) = \int_{-1}^{1} p_{\rm ring}(x,\, \mu_i) d\mu_i. \tag{21}$$

Let us assume that the magnetic field does not depend on latitude but radius only, so that its magnitude and direction are constant everywhere on the shell. Using the normalized expressions for $p_{\rm ring}$ from Table 2, we evaluate equation (21) for each of the five special cases discussed in the previous section. The results are listed in Table 3. For radial and axial magnetic fields, the polarization is zero, since $p_{\rm ring}$ has no Hanle effect. In contrast, the meridional and cylindrical radial field distributions both yield a net polarization that is proportional to the product of $\sin^2 i$ and $\sin^2 \alpha_2$. A toroidal field yields the same result for the polarization but with a minus sign, hence the polarization position angle is perpendicular to Z_* instead of parallel as in the cases of B_ϑ and B_ρ. The expressions of Table 2 have the proper limit that when $B = 0$ (i.e., $\alpha_2 = 0$), the polarization from the shell vanishes. It is also interesting that the maximal polarization occurs for large magnetic field strengths (i.e., $\alpha_2 \to \pi/2$). We point out, however, that the $\sin^2 \alpha_2$ dependence is valid only for these special cases and may not result for general field distributions.

TABLE 3

ANALYTIC EXPRESSIONS FOR THE HANLE EFFECT IN SPHERICAL SHELLS

Field Type	Integrated Line Polarization
$B = 0$.....	0
B_r.....	0
B_Z	0
B_ρ	$\sin^2 i \sin^2 \alpha_2$
B_ϑ	$\sin^2 i \sin^2 \alpha_2$
B_φ	$-\sin^2 i \sin^2 \alpha_2$

To compute the polarization from a spherical envelope, the contributions from shells at different radii must be summed. This is accomplished through a radial integration of equation (21), giving

$$p_{\rm sph} = \int_1^\infty p_{\rm shell}(x) dx\ . \tag{22}$$

Note that for our special cases, it is $\sin^2 \alpha_2$ that is a function of radius through its dependence on the magnetic field distribution.

To illustrate the polarization expected from spherical envelopes, we have calculated $p_{\rm sph}$ for several different magnetic field geometries and show the results in Figure 6. The density in the wind is taken to be the power law of the previous section with $t = 0$, hence $\tilde{n} \sim x^{-2}$. The four curves correspond to envelopes with meridional, toroidal, dipolar, and quadrupolar magnetic field distributions. As in the previous section, the field strength for both the meridional and toroidal fields is assumed to be a power law in radius with $m = 1$, and thus $B \sim x^{-1}$. The dipole field is given by

$$B_r = \frac{2B_* \cos \vartheta}{x^3}\ ,$$

$$B_\vartheta = \frac{B_* \sin \vartheta}{x^3}\ ,$$

$$B_\varphi = 0\ .$$

Note that B_* in the dipole case is defined to be the surface magnetic field strength at the equator. Relative to the equator, the surface magnetic field at the pole is twice as strong. For the quadrupole, the magnetic field components are

$$B_r = \frac{-B_* \cos 2\vartheta}{x^4}\ ,$$

$$B_\vartheta = \frac{-B_* \sin 2\vartheta}{x^4}\ ,$$

$$B_\varphi = 0\ .$$

An important point to note is that even for the more geometrically complicated distributions of dipole and quadrupole field distributions, the net line polarization is still proportional to $\sin^2 i$. This proportionality has persisted for every field distribution that we have tried, and we have considered magnetic field orientations with various combinations of $\vartheta_B = 0°$, 15°, 45°, 75°, and 90°, $\varphi_B = 0°$, 15°, 45°, 75°, and 90°, $\alpha_2 = 0°$, 15°, 45°, 75°, and 90°, and for rings at latitudes $\vartheta = 0°$, 15°, 45°, 75°, and 90°. In each of these tests, the polarization was computed at inclinations ranging from pole-on to edge-on at 10° intervals.

Returning to the discussion of spherical envelopes, Figure 6 shows that the meridional and toroidal fields yield the same polarization in magnitude but differ by a sign. The Hanle effect for both the dipole and quadrupole fields yield positive polarizations with position angles like that for B_ϑ, but with smaller magnitudes; however, the Hanle effect for the dipole field is significantly stronger than that for the quadrupole. There are two factors contributing to differing

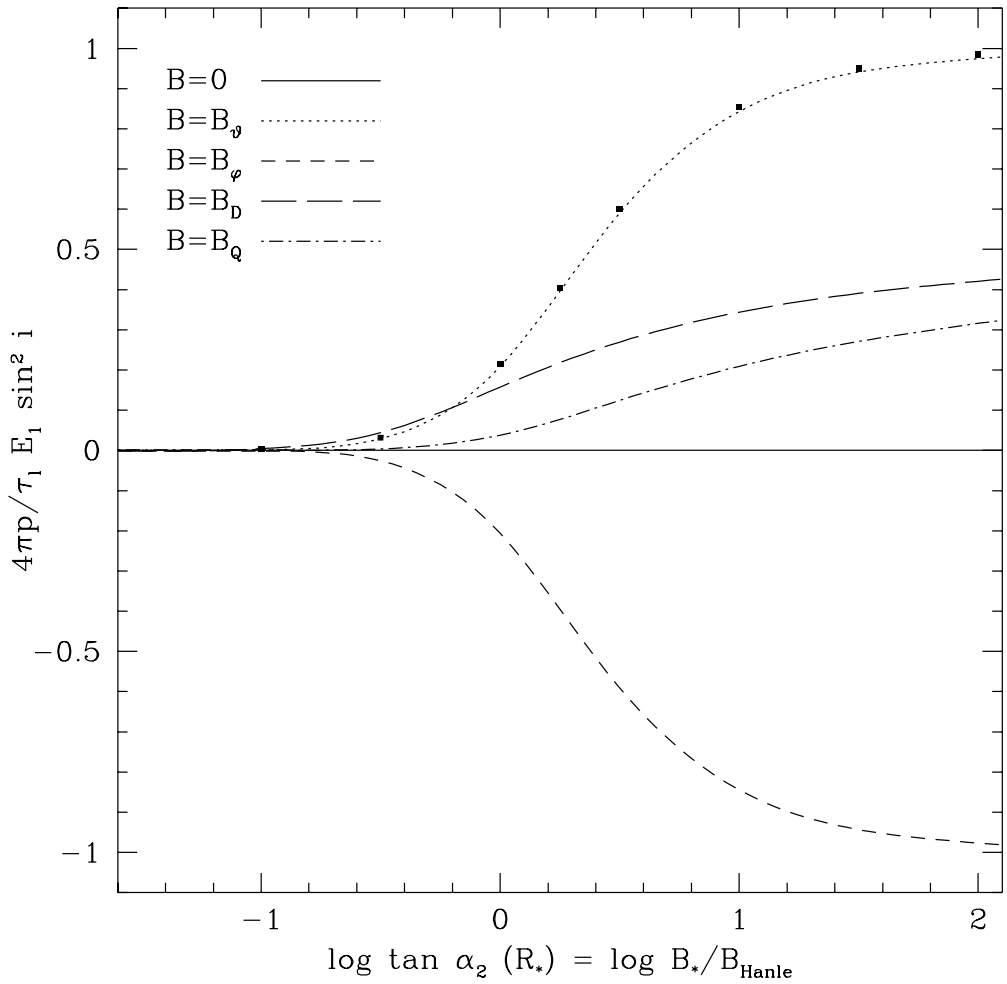

FIG. 6.—The Hanle effect for spherical envelopes. Shown are four computed curves, each for a different magnetic field geometry, as indicated in the figure. The square points mark the analytic solution to the case of $B = B_\vartheta$ and give an indication of the numerical accuracy. The vertical and horizontal axes are the same as in Fig. 5. The latitudinal and toroidal fields produce polarizations that are the same in magnitude but opposite in sign, indicating a difference of 90° in the polarization position angle. The dipole and quadrupole fields produce successively smaller variations of the polarization at large values of $B_*/B_{\rm Hanle}$. The polarization for the dipole and quadrupole fields does not obtain values as large as those for latitudinal or toroidal fields, for reasons that are discussed in the text.

results for the various field distributions: (1) the radial dependence of the field strength and (2) the directional dependence of the magnetic field with latitude. In the first the magnetic field is expected to decrease with radius. If the field strength decreases rapidly with radius, then a significant Hanle effect will occur only in a small fraction of the scattering volume in the innermost regions, where the field strength is greatest. Fortunately, most of the polarization is produced at small radii, where the density of scatterers is largest; thus, even when the field strength strongly decreases with radius, the Hanle effect may still appreciably affect the observed line polarization. For example, of the cases considered, the decrease of field strength with radius is severest for the quadrupole distribution, and the deviation of the polarization at large field limits is smallest in comparison to the other field distributions. As the field strength is made to decrease more gradually with radius (e.g., the dipole field case), the Hanle effect is significant over a greater range of radii.

The second factor that governs the importance of the Hanle effect is the vector direction of the magnetic field as a function of latitude. If the magnetic field tends to be radial or axial over significant ranges of latitude, then there will be little Hanle effect in those regions. For example, a quadrupolar distribution has primarily radial magnetic fields at the equator and poles but a strongly latitudinal orientation at midlatitudes. The dipole configuration is similar, with a dominant radial component near the poles but an axial component at the equator. Clearly, magnetic fields that are dominated by radial or axial components will reduce the importance of the Hanle effect for producing a net polarization in spherical envelopes, thereby reducing the likelihood of confidently detecting the magnetic field and ascertaining its distribution in such cases. Thus, for integrated polarized line profiles, radial and axial fields are effectively undetectable using the Hanle effect.

Several conclusions may be drawn from our consideration of magnetic fields embedded in spherical envelopes. First, the example of spherical envelopes provides an ideal demonstration of how the Hanle effect can produce a net polarization, in contrast to a depolarization. Second, the Hanle effect tends to be more significant for magnetic fields that decrease gradually with radius, or at least that decrease gradually in the regions close to the star where contributions to the polarization are greatest. And third, the field component should have significant meridional and/or

toroidal field components for the integrated line polarization to be modified by the Hanle effect.

4. DISCUSSION AND OBSERVATIONAL PROSPECTS

To this point the Hanle effect has been introduced, and its theoretical consequences for the line polarization of extended stellar envelopes explored. Here the use of these results to interpret observations is discussed. From Figures 5 and 6, the most dramatic change in the line polarization relative to the zero field case occurs when the Hanle effect is in the saturated limit, so we elaborate on the case of large field strengths in some detail. Attention is then shifted toward possible stellar targets and the selection of resonance-lines to be observed. Lastly, a procedure is introduced for determining stellar magnetic fields from line polarimetric observations using our theoretical results.

4.1. *The Limit of Very Large Field Strengths*

Recall that in the zero field limit, the Hanle phase scattering matrix reduces to that of simple resonance-line scattering, which for the most part is quite similar to that of electron scattering in its functional form. It is natural, therefore, to consider the opposite extreme in which the magnetic fields are very strong.

"Large magnetic fields" refer to the regime where $\omega_L \gg A_{ul}$, yet $\Delta v_Z \ll \Delta v_D$. In this limit the Hanle parameter becomes $\tan \alpha_2 \to \infty$, hence the Hanle angle $\alpha_1 \approx \alpha_2 \approx \pi/2$. Using equation (A3) of the Appendix, the relevant phase matrix elements reduce to $H_{QI} = \frac{3}{8}E_1 \sin^2 \theta_s(1 - 3 \cos \theta_i^2)$ and $H_{UI} = 0$. However, these angular parameters are with reference to the magnetic field direction. To solve equation (16) for the ring polarization, the integrand must be expressed in terms of the stellar coordinates. The quantities θ_s, θ_i, and i_s can be eliminated in favor of the stellar coordinates ϑ_B, φ_B, and φ_i and the viewing inclination $\vartheta_s = i$ by using the spherical triangles in Figure 4. The following coordinate transformations are derived:

$$\cos \theta_s = \cos i \cos \vartheta_B + \sin i \sin \vartheta_B \cos \varphi_B , \quad (23)$$

$$\cos \theta_i = \cos \vartheta_i \cos \vartheta_B + \sin \vartheta_i \sin \vartheta_B \cos (\varphi_i - \varphi_B) , \quad (24)$$

$$\cos i_s = \frac{\cos \vartheta_B - \cos i \cos \theta_i}{\sin \theta_s \sin i} , \quad (25)$$

$$\sin i_s = \frac{\sin \varphi_B \sin \vartheta_B}{\sin \theta_s} . \quad (26)$$

It is also convenient to parameterize the azimuth of the magnetic field by $\varphi_B = \varphi_i - \psi_0$, where ψ_0 is defined to be a "phase." We introduce this substitution because equation (16) requires an integration about the ring with respect to φ_i. The assumption of axisymmetry ensures that ψ_0 is constant around the ring. Clearly, if $\psi_0 \neq 0$, then the magnetic field has some toroidal component, otherwise the magnetic field lies only in meridional planes containing the axis of symmetry.

Using H_{QI} and H_{UI} with the geometrical expressions (23), (24), (25), and (26) and performing the integral of equation (16), the analytic solution for the line polarization from a strongly magnetized ring is

$$p_{\rm ring}(\alpha_2 = \pi/2) = \tfrac{3}{16}\tau_l E_1 \sin^2 i \,(1 - 3 \cos \theta_i^2) \times (1 - \tfrac{3}{2} \sin^2 \vartheta_B) . \quad (27)$$

For the sake of compactness, we have not substituted the coordinate transformation (24) for $\cos \theta_i$ with $\varphi_i - \varphi_B = \psi_0$ in equation (27). We make three observations regarding the ring polarization with a strong magnetic field:

1. The ring polarization is proportional to $\sin^2 i$, just as in the zero field case of Brown & McLean (1977) and in the semianalytic cases discussed in the previous section.
2. The effects of a toroidal field enter only through $\cos \theta_i = \cos \vartheta_i \cos \vartheta_B + \sin \vartheta_i \sin \vartheta_B \cos \psi_0$, with $\cos \theta_i$ being the cosine of the angle between the incident intensity and the magnetic field, *not* the stellar symmetry axis.
3. At a fixed value of $\cos \theta_i$, the polarization can actually change signs (i.e., a 90° flip in the polarization position angle) at a critical value of ϑ_B.

Regarding the third point, the critical value of ϑ_B can be derived by setting $p_{\rm ring} = 0$ in equation (27) and solving for ϑ_B. These steps yield

$$\vartheta_B^{\rm crit} = \sin^{-1} \sqrt{\tfrac{2}{3}} = 54.^{\circ}7 . \quad (28)$$

Recall that 54.°7 is the van Vleck angle. In the zero field case, a ring located at exactly this latitude will have no net polarization. Equation (28) indicates something quite different in the case of a strong magnetic field: if the orientation of the magnetic field is such that ϑ_B equals the van Vleck angle, then the ring will have zero net polarization *independent* of the ring's latitude.

The results derived in this section for the polarization from a ring in the large field limit are particularly relevant for the discussion of observations that follows in the next two sections. First, as previously alluded to, it is in the limit of strong fields that the line polarization is seen to deviate most from that of the zero field case. Second, we have derived analytic results for any axisymmetric field geometry in the strong field case. Although derived for a ring only, the result may easily be extended to envelope volumes by integrating the rings over latitude. Thus, the asymptotic properties of the line polarization for strong fields is governed by the field geometry, a conclusion that will be utilized later for diagnosing the stellar magnetic field properties from several polarimetric line measurements.

4.2. *Observational Prospects*

The parameter τ_l that is implicitly defined by equation (15) for the frequency mean Sobolev optical depth is of central importance for determining the net line polarization from optically thin stellar envelopes. This factor sets the scale of the polarization and depends on the stellar properties, wind parameters, and the particular resonance-line transition. A critical assumption used in constructing the theoretical curves shown in Figures 5 and 6 for the line polarization is that the line must be optically thin. We wish to determine which lines in which stars will meet this condition. Recall that

$$\tau_l = \frac{\lambda_{ul} \sigma_l R_* n_0}{2 v_\infty} . \quad (29)$$

For a stellar wind, we define the number density normalization by

$$n_0 = \frac{X \mathscr{A}_E q_i \dot{M}}{4\pi R_*^2 v_\infty \mu m_{\rm H}} . \quad (30)$$

In equation (30), X is the hydrogen mass fraction by weight, $\mathscr{A}_E$ is the elemental abundance by mass, q_i is the constant ionization fraction, and $\dot{M}$ is the stellar mass-loss rate. Combining expressions (29) and (30) with the fact that $\sigma_l \propto \lambda_{ul}^2 A_{ul}$ gives $\tau_l \propto X \mathscr{A}_E q_i \dot{M} \lambda_{ul}^3 A_{ul}/R_* v_\infty^2$. Thus, conditions that are favorable for producing optically thin lines include (1) winds that have small mass-loss rates or high terminal speeds, (2) atomic species that have low abundances, or (3) lines that are formed by trace ions. Note that τ_l would appear to depend quite strongly on the wavelength of the line; however, A_{ul} is also wavelength dependent and varies as $\lambda_{ul}^{-2} g_l f_{lu}/g_u$, where f_{lu} is the oscillator strength of the upward transition. For values typical of strong lines from hot star winds, we rewrite τ_l in the normalized form:

$$\tau_l = 0.35 \frac{\lambda_{ul,3}\, \sigma_{l,-3}\, R_{*,1}\, n_{0,4}}{v_{\infty,3}}, \tag{31}$$

where

$$n_{0,4} = 0.63 \frac{X(\mathscr{A}_E q_i \dot{M})_{-13}}{\mu R_{*,1}^2 v_{\infty,3}}. \tag{32}$$

The subscripted numbers indicate powers-of-ten normalizations, with λ_{ul} in angstroms, σ_l in cm^2 Hz, R_* in $R_\odot$, n_0 in cm^{-3}, v_∞ in km s^{-1}, and $\dot{M}$ in $M_\odot$ yr^{-1}.

An upper limit to the value of τ_l is found by considering the case in which every photon emitted by the star in the frequencies of the line is scattered at least once. The Stokes I flux produced by the scattered photons only is roughly $\tau_l \Delta\nu_L L_\nu/4\pi d^2$ times a function of geometry that is close to unity. By inspection τ_l should be about one or less to avoid multiple scattering in the envelope. As a result, equation (31) can be used as a criterion for the selection of stellar candidates and resonance lines to be observed. Note that the maximum polarization (for a *point-source star*) is of order 20% (τ_l); hence, for stars with magnetic winds, one expects to measure intrinsic line polarizations with typical values of several percent for optically thin lines. These estimates assume that $E_1 \approx 1$ and that the star is viewed edge-on. It is important to note that the inclusion of finite star effects is expected to reduce significantly, relative to the point star case, the maximal polarization that can be produced in an optically thin wind (see Cassinelli et al. 1987).

Requiring that $\tau_l \lesssim 1$, constraints are placed on the various wind and stellar parameters for which our optically thin results will be relevant. To order of magnitude, a resonance line formed in a typical hot star wind will be optically thin if $\mathscr{A}_E q_i \dot{M} \lesssim 10^{-13} M_\odot$ yr^{-1}. Although the product $\mathscr{A}_E q_i$ may vary greatly between different lines, it can at most be of order 10^{-4} for the dominant ionization state of abundant metals in stars with solar abundances. So for lines from dominant stages to be optically thin, $\dot{M}$ must be about $10^{-9} M_\odot$ yr^{-1} or less, values that may have relevance for some B star winds. However, if we consider lines of trace ions that have $q_i \ll 1$ and/or atomic species with smaller abundances $\mathscr{A}_E$, then the Hanle diagnostic can be used for resonance lines in winds with considerably larger values of $\dot{M}$.

A careful selection of targets that are thought to possess magnetic fields of tens and hundreds of gauss may allow for the detection of the Hanle effect in stars other than the Sun. Estimates of τ_l for several early-type stars are given in Table 4 (below). Included in the list are Wolf-Rayet stars, O stars, and emission line B stars. For each candidate, only one commonly observed line is selected for computing τ_l. It can be seen that optically thin lines can be found in a wide variety of hot star winds.

In particular for the B stars, the class of helium weak and helium strong stars have surface magnetic fields of kilogauss strengths (Borra & Landstreet 1979). These objects are typically modeled as oblique magnetic rotators (see Shore 1987), for which the stellar magnetic field is dipolar, but with a symmetry axis that is not aligned with the star's rotation axis. Shore suggests that the dipole fields (1) inhibit wind flow at latitudes near the equator and (2) collimate a bipolar jet. Although the surface field strengths are somewhat strong, these helium peculiar B stars might provide a good test for the optically thin results presented here, since the wind density is relatively small and some information already exists about the magnetic and stellar geometries.

4.3. *Diagnosing Stellar Magnetic Fields with the Hanle Effect*

Here we address the issue of how polarimetric line measurements can be combined with our theoretical results to diagnose the magnetic strength and geometry in extended stellar envelopes. The procedure described below is schematic and rather idealized; the analysis of real data will be more complicated if our simplifying assumptions are found to be invalid.

The strategy that we propose for deriving the magnetic field properties from polarimetric line measurements is similar to curve-of-growth theory. Relative abundances of different atomic species may be derived from the curve of growth by plotting the ratio W_λ/λ, where W_λ is the line equivalent width, versus the line's oscillator strength, or f-value (note that the f value and the A_{ul} value are directly related). For example, the horizontal shift between the curves of growth for two atomic species will yield the relative abundance of those atoms. For the case of the Hanle effect, the procedure is to plot a suitably normalized line polarization versus the A_{ul} value.

Let us suppose that we have low spectral resolution or perhaps narrowband polarimetric measurements of a sequence of resonance lines. As an example, Figure 5 shows five lines commonly observed in hot star winds: Si III, Si IV, C IV, N V, and P V. The atomic data for the line transitions of interest are listed in Table 5 (see also Table 4). Also listed in this table are basic data for many other lines that are not used in our discussion but are conveniently included for use in the future planning of observations. The various columns of Table 5 are the transition states, the wavelength, the value of E_1, and the Hanle field strength, $B_{\rm Hanle}$. Note that several of the selected lines are doublets, and of these doublets, only the short-wavelength components are polarized while the long wavelength components scatter isotropically. Note that for these doublets, E_1 is not actually a constant but can be frequency dependent, because there exists a quantum mechanical interference effect between the doublet components that can alter the line polarization (Stenflo 1980). We have chosen to ignore this effect, since only optically thin lines are being considered here. An additional concern involving the doublets is that the two line components may be blended because of the wind broadening. Although we also ignore this possibility, such blends are quite common in the fast winds of O stars, but less so in the slower B star winds. Of course, even in singlets, blends with other nearby lines is a concern.

TABLE 4

A Selection of Stars and Lines for Observing the Hanle Effect

Stellar Class	Line	log $\mathscr{A}_E$	log q_i[a]	log $\dot{M}$ ($M_\odot$ yr^{-1})	v_∞ (10^3 km s^{-1})	R_* ($R_\odot$)	τ_l
WN6.....	P v 1118 Å	−5.50	−2	−4.5	2000	5	0.70
OV.....	Si III 1207 Å	−4.46	−3	−6.0	2000	10	0.70
B1 I.....	N v 1239 Å	−3.96	−3	−6.0	1400	40	0.10
B2 V.....	Si IV 1394 Å	−4.46	−2	−9.0	800	7	0.02

[a] The ionization fraction is a parameter of great uncertainty, so only estimates of its value are given.

Referring back to Figure 5, we now discuss the arrow markers shown at the bottom of that figure that represent the horizontal positions of polarimetric measurements for different lines, as indicated. The relative positions of these markers are fixed, because for a given field strength, the spacing of the arrows depends only on the ratio of the line A_{ul} values. The positions shown in Figure 5 have been computed assuming a surface field $B_* = 100$ G. A change in B_* will move the entire ensemble of arrows either left (for smaller B_*) or right (for larger B_*).

Now to use Figure 5, we want to plot the polarization for each line that is horizontally spaced according to the arrow markers and fit the distribution of points to the diagnostic curves. However, lines of different species have different abundances, and those of the same species but of different ionizations stages will have different ionization fractions. For a given stellar wind, it is the abundance and ionization fractions (as well as level populations for different lines of the same ion) that differentiate the line optical depth between different lines, but these differences are characterized by the parameter τ_l. For this reason it is not the polarization p that we plot, but instead it is $p/E_1\,\tau_l \sin^2 i$, where $\sin^2 i$ is a constant for every line and $E_1\,\tau_l$ will vary from line to line. The result is that given our assumptions, the ratio $p/E_1\,\tau_l \sin^2 i$ should be a constant in the absence of magnetic fields.

TABLE 5

Magnetic Sensitivities in Common Resonance Lines

Ion	Transition[a]	λ (Å)	E_1	A_{ul}[a] (10^8 s^{-1})	$B_{\rm Hanle}$ (G)
O VI.....	$2\,^2S_{1/2}$–$2\,^2P_{3/2}$	1031.9	0.5	4.163	18
O VI.....	$2\,^2S_{1/2}$–$2\,^2P_{1/2}$	1037.6	0.0	4.095	...
P V.....	$3\,^2S_{1/2}$–$3\,^2P_{3/2}$	1118.0	0.5	12.63	54
P V.....	$3\,^2S_{1/2}$–$3\,^2P_{1/2}$	1128.0	0.0	12.29	...
Si III.....	$3\,^1S_0$–$3\,^1P_1$	1206.5	1.0	25.5	145
N V	$2\,^2S_{1/2}$–$2\,^2P_{3/2}$	1238.8	0.5	3.411	15
N V	$2\,^2S_{1/2}$–$2\,^2P_{1/2}$	1242.8	0.0	3.378	...
Si IV.....	$3\,^2S_{1/2}$–$3\,^2P_{3/2}$	1393.8	0.5	8.825	38
Si IV.....	$3\,^2S_{1/2}$–$3\,^2P_{1/2}$	1402.8	0.0	8.656	...
C IV	$2\,^2S_{1/2}$–$2\,^2P_{3/2}$	1548.2	0.5	2.654	11
C IV	$2\,^2S_{1/2}$–$2\,^2P_{1/2}$	1550.8	0.0	2.641	...
Mg II.....	$3\,^2S_{1/2}$–$3\,^2P_{3/2}$	2796.4	0.5	2.612	11
Mg II.....	$3\,^2S_{1/2}$–$3\,^2P_{1/2}$	2803.5	0.0	2.592	...
Ca II	$4\,^2S_{1/2}$–$4\,^2P_{3/2}$	3934.8	0.5	1.367	6
Ca II	$4\,^2S_{1/2}$–$4\,^2P_{1/2}$	3969.6	0.0	1.331	...
Ca I	$4\,^1S_0$–$4\,^1P_1$	4227.9	1.0	2.180	12
Na I.....	$3\,^2S_{1/2}$–$3\,^2P_{3/2}$	5891.6	0.5	0.606	3
Na I.....	$3\,^2S_{1/2}$–$3\,^2P_{1/2}$	5897.6	0.0	0.610	...
K I	$4\,^2S_{1/2}$–$4\,^2P_{3/2}$	7667.0	0.5	0.387	2
K I	$4\,^2S_{1/2}$–$4\,^2P_{1/2}$	7701.0	0.0	0.382	...

[a] The transition and Einstein A value taken from Morton 1991.

The following procedure may be used to derive the magnetic field strength B_* and the field geometry. (1) In Figure 5, the polarization measurements are to be vertically scaled and the distribution allowed to slide horizontally until a best fit is achieved to one of the theoretical curves (remember that the relative horizontal spacing of the measurements is fixed). This best fit provides the surface field strength from the abscissa and the field geometry from the distribution. The fit also provides the ratio $p/E_1\,\tau_l \sin^2 i$. Since p is measured and E_1 is known from theory, the product $\tau_l \sin^2 i$ is made known through the scaling parameter that was required to obtain a best fit to one of the diagnostic curves. In principle, τ_l and $\sin^2 i$ may be determined individually by fitting the Stokes I profile of the line, because the profile shape and the total emission depend on the line optical depth and viewing perspective. Additionally, these τ_l and $\sin^2 i$ values are also related to the vertical intercept of Figure 5 in the limit of $B_*/B_{\rm Hanle}$, as is discussed further below.

For interpreting the best-fit case, the diagnostic curves of Figure 5 can be divided into three principle regions: $B_*/B_{\rm Hanle} \ll 1$, $B_*/B_{\rm Hanle} \gg 1$, and $B_*/B_{\rm Hanle} \approx 1$. These three divisions are shown schematically in Figure 7. First, for the lines with $B_*/B_{\rm Hanle} \ll 1$, the Hanle effect is almost negligible, and the line measurements will be found toward the far left of Figure 7. In this case the magnitude of the net line polarization is related to the density distribution throughout the envelope. The position angle of the polarization on the sky is set by the distribution of scatterers. Under the assumption of axisymmetry, the position angle indicates the orientation of either the symmetry axis (for a plume) or the equator (for a disk). The resolution of this ambiguity may be found either by requiring consistency with the fits to the Stokes I profile or with other observations, if available (such as the imaging of a jet or of an absorption band as expected from an occulting disk). Thus, resonance lines with small ratios of $B_*/B_{\rm Hanle}$ are generally useful for constraining the envelope density distribution.

For polarization measurements in the regime of $B_*/B_{\rm Hanle} \gg 1$, the data points will be located toward the far right of Figure 7. In this area the Hanle effect is in the saturated limit, so the line becomes insensitive to the field strength. However, the degree of polarization is still sensitive to the geometry of the magnetic field and its distribution throughout the envelope. In particular, a 90° position

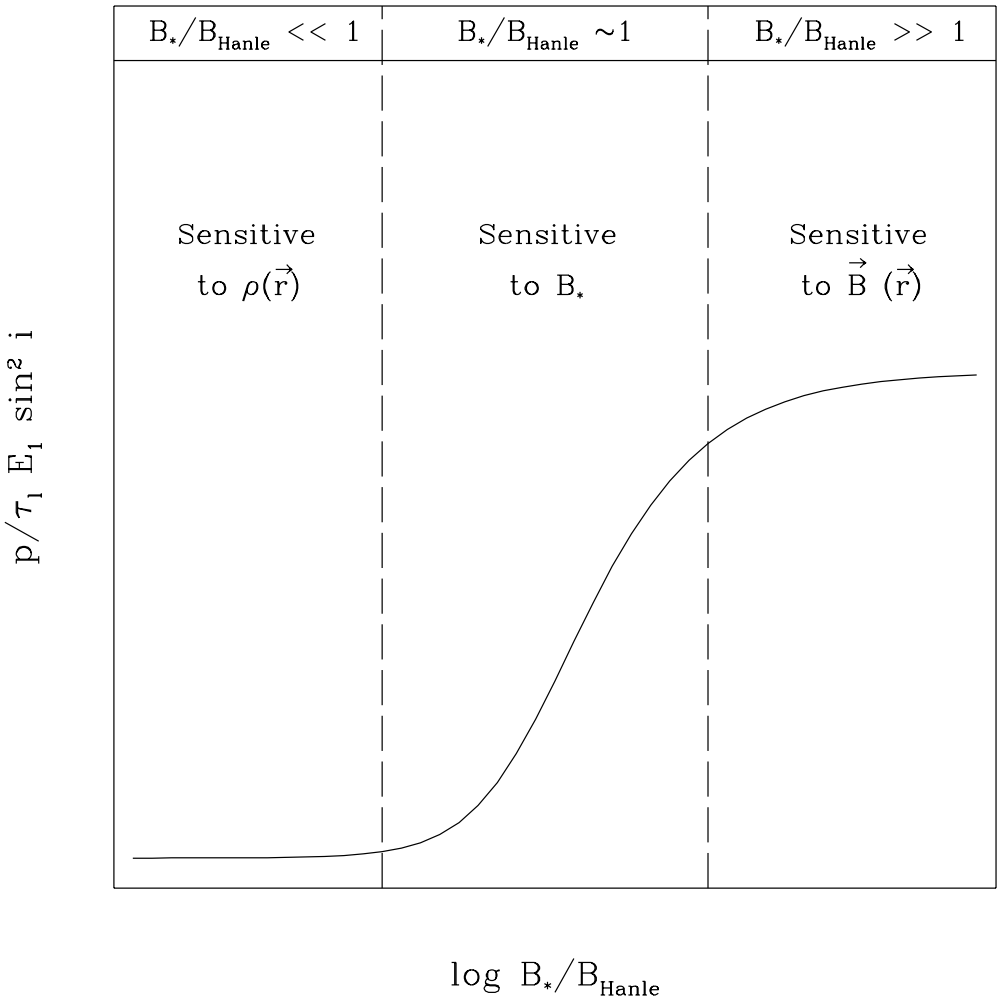

FIG. 7.—Diagnostic sensitivities for three limits of the ratio $B_*/B_{\rm Hanle}$. This figure presents a summary of how our theoretical results may be used to derive the magnetic properties of a stellar envelope. Plotted is the normalized line polarization (as in Figs. 5 and 6) as a function of $B_*/B_{\rm Hanle}$ for a fictitious field distribution (shown only for reference). The space is divided into three regions, corresponding to $B_*/B_{\rm Hanle} \ll 1$ (*left*), $B_*/B_{\rm Hanle} \sim 1$ (*middle*), and $B_*/B_{\rm Hanle} \gg 1$ (*right*). As discussed in the text and as indicated in the figure, the regimes of (1) small $B_*/B_{\rm Hanle}$ ratios provide information about the envelope density distribution, (2) large $B_*/B_{\rm Hanle}$ ratios give an indication of the vector magnetic field geometry, and (3) $B_*/B_{\rm Hanle}$ ratios near 1 are useful for deriving the surface field strength.

angle change of the polarization would provide strong evidence for the presence of a magnetic field, assuming that the ions producing the polarization are all located in the same region. When combined with a line measurement that lies in the regime of $B_*/B_{\rm Hanle} \ll 1$, the saturated case can provide information about the field geometry and can be used to set a lower limit to the surface field strength.

Finally, the third important region in Figure 7 is for the case of $B_*/B_{\rm Hanle} \sim 1$. It is in this area of the figure that the diagnostic curve makes the transition from the zero field limit to the saturated limit, as illustrated by the nonzero slope of the curve. In the two extreme cases, the surface field strength of the star cannot be reliably determined, but limits may be placed on its value. However, if one or more polarimetric line measurements fall into the intermediate regime between small and large $B_*/B_{\rm Hanle}$ ratios, then those lines can be used to determine the surface field strength.

The two most important conclusions to be drawn from this discussion of Figure 5 are the following. (1) At least two lines must be used to determine whether or not the Hanle effect is observed, unless other information is available to reduce the number of free parameters. If both lines are formed in the same geometrical region and there is no magnetic field, then the two lines should have the same polarization and position angle. A difference in either of these could be an indication of the Hanle effect in operation. (2) It is clear that the greatest diagnostic value of the Hanle effect will come from multiline measurements, with a greater number of lines providing tighter constraints on the circumstellar magnetic field properties. Not only are the sheer number of lines important, but also the sensitivity coverage of the lines to the magnetic field strength, since B_* is a priori unknown. For example, if the arrow markers had been computed for $B_* = 1000$ G instead of 100 G, then all of the line polarizations would have been in or nearly in the saturated limit. The field geometry could be derived, but only lower limits could be placed on the surface field strength. However, even lower limits would be useful. Similarly, if B_* were only 1 G, then all of the line measurements would shift leftward in Figure 5, so that little could be derived about the field geometry, yet an upper limit could be placed on the B_* value.

We recognize that our examples are certainly simplified, and we wish to point out some of the complicating factors that should be accounted for. Theoretically, a constant ionization fraction was assumed in producing Figure 5. An ionization fraction that is constant throughout the wind will not generally be the case; moreover, the ionization distribution for different ions will also not be the same. Finite star effects have been ignored. These include the finite size of the star, limb darkening, the presence of photospheric distortions (e.g., oblateness), and other atmospheric effects. And of course, only rather simple magnetic field distributions have been investigated, whereas the true magnetic topology may be much more complex.

Observationally, we identify several possible complications with interpreting the spectral line measurements. The first is that line blending may occur between nearby lines or adjacent multiplet components because of wind broadening. The line polarization will likely be altered at the frequencies of overlap because of the enhanced opacity. A second complication is that of contamination of the line polarization from processes other than the resonance-line scattering. An example would be electron scattering; however, note that in hot star winds τ_e is usually thin for mass-loss rates below $10^{-6}\ M_\odot\ \mathrm{yr}^{-1}$. Although the continuum polarization arising from electron scattering (or even from interstellar polarization processes) can be separated from the line polarization component through continuum subtraction, the polarized line profile may be distorted by Doppler shift effects due to electron scattering (Wood & Brown 1994b).

Even though there are many effects that must be properly modeled, our simplified considerations have demonstrated that the Hanle effect could be a useful probe of the gross magnetic properties of extended stellar envelopes. Such information is difficult or impossible to obtain by other means, especially in the regime of only tens to hundreds of gauss. It is hoped that the Far Ultraviolet Spectro-Polarimeter (FUSP), a rocket payload to be launched in the near future, will observe the Hanle effect for the first time in a star other than the Sun. This instrument will have a spectral resolution of $\lambda/\Delta\lambda \approx 1000$ in the wavelength range 1050–1450 Å. FUSP is expected to obtain observations of the Wolf-Rayet star EZ CMa and the Be star π Aqr, both of which are known to be intrinsically polarized.

5. SUMMARY

In this study we have considered applications of the Hanle effect as a diagnostic of magnetic fields for extended stellar envelopes. The polarizing effects of resonance-line scattering in an optically thin envelope illuminated by a point-source star have been investigated, and our results can be reduced to three major points.

1. Because the polarization is given by a Rayleigh scattering phase function, the dependence of the line resonance polarization on the envelope geometry is the same as for the case of pure electron scattering. The main differences between these two processes are (a) the line opacity can be larger than the electron scattering opacity by many orders of magnitude, (b) the line opacity is frequency dependent, and (c) although resonance-line scattering is basically of the Rayleigh type, the polarization is diluted by an isotropic contribution. In the zero field limit, the envelope polarization arising from either electron scattering or resonance-line scattering varies with the line-of-sight viewing angle as $\sin^2 i$. Analytic solutions to several simple cases reveal that this $\sin^2 i$ dependence persists even when there is a magnetic field. From numerical calculations for a variety of magnetic field orientations, we argue that the $\sin^2 i$ dependence is a general result for optically thin magnetic winds. From numerical calculations, the $\sin^2 i$ dependence of the *net* line polarization is found to exist for axisymmetric rings at various latitudes, for magnetic fields of various strengths, and for a broad range of field orientations. As a result, the polarization from *any* axisymmetric envelope must be proportional to $\sin^2 i$, just as in the zero field case.

2. The calculation of the Hanle effect for observed line polarizations generally requires a numerical integration of a complicated function of the magnetic field geometry and the density distribution over the scattering envelope. Analytic results can be derived only for simplified geometries. In particular, we considered axisymmetric rings (a) for arbitrary field geometries but in the limit of very strong field strengths and (b) for geometrically simple field distributions (e.g., radial, axial, etc.) but of arbitrary strength. In favorable cases the Hanle effect can produce significant changes in the degree of polarization, relative to the zero field case. Some field distributions can even result in a position angle flip of 90°. Although the Hanle effect may cause a net reduction of the envelope polarization, it can also increase or create a net polarization. For example, in the absence of magnetic fields, a spherical envelope should be unpolarized; however, a magnetic field can break this symmetry to yield a net polarization. Typically, meridional magnetic fields are found to yield polarizations that are aligned with the stellar axis, whereas fields with a significant toroidal component tend to produce net polarizations that are perpendicular to that axis.

3. Lastly, potential stellar targets were discussed. Resonance lines of highly ionized species, such as C IV, Si IV, and others, are commonly observed in the winds from hot stars, and polarimetric measurements of these lines should be used together to infer the stellar magnetic field strength and distribution. Note that this research has been motivated by the upcoming FUSP experiment that will observe hot stars at UV wavelengths, but the Hanle effect pertains generally to resonance-line scattering, so the effect can also be observed using ground-based telescopes. The optically thin results that we have derived for the Hanle effect require relatively small values of $\dot{M} q_i \mathscr{A}_E$ and/or large terminal speeds v_∞. The best hot star candidates under these conditions are likely the O and B stars, because they have numerous UV resonance lines and their wind mass-loss rates are not exceedingly large. In particular, the helium peculiar magnetic B stars may provide a good test for our diagnostic because in some cases the stellar field strengths and distributions have already been studied.

In conclusion, the diagnostic value of the Hanle effect for stellar observations appears promising. The fact that the Hanle effect can probe magnetic field strengths in the sub-kilogauss range, values that may be common in stellar atmospheres, motivates a continued study of this effect. Some considerations that should be included in the future are the effects of a finite star and large optical thickness. Although we have considered rather simplified cases, our results for optically thin atmospheres provide a good start

for employing the Hanle effect in studies of stars other than the Sun.

The authors gratefully acknowledge helpful discussions with Dave Clarke, Jon Bjorkman, Charles Goebel, John Brown, Barbara Whitney, Art Code, and Kenny Wood. Finally, we thank the referee, Jan Stenflo, for several useful comments. This research was supported by NASA grant NAG 5-2854.

APPENDIX

THE HANLE EFFECT PHASE MATRIX

In this Appendix the definition of the Hanle effect phase matrix is presented. It is this phase matrix that determines the Stokes parameters for resonance-line scattering in a magnetic medium. Recall from equation (11) that the 4-vector source function is given by

$$\boldsymbol{S}_v = \begin{pmatrix} S_I \\ S_Q \\ S_U \\ S_U \end{pmatrix} = \frac{1}{4\pi} \int L(i_2) H(\boldsymbol{n}_i, \boldsymbol{n}_s) L(i_i) \boldsymbol{I}_{v,i} \, d\Omega \, . \tag{A1}$$

In this expression $\boldsymbol{I}_{v,i}$ is the incident Stokes vector, which will generally have nonzero values for Q, U, and V. After doing the matrix addition of equations (5.57)–(5.64) in Stenflo (1994), the Hanle scattering phase function is

$$H(\boldsymbol{n}_i, \boldsymbol{n}_s) = \begin{pmatrix} H_{II} & H_{IQ} & H_{IU} & H_{IV} \\ H_{QI} & H_{QQ} & H_{QU} & H_{QV} \\ H_{UI} & H_{UQ} & H_{UU} & H_{UV} \\ H_{VI} & H_{VQ} & H_{VU} & H_{VV} \end{pmatrix}, \tag{A2}$$

where $\boldsymbol{n}_i$ and $\boldsymbol{n}_s$ represent the directions of the incident and scattered intensities. The matrix elements appearing in equation (A2) are

$$\begin{aligned}
H_{II} &= 1 + \tfrac{3}{4} E_1 [\tfrac{1}{6}(1 - 3\cos^2\theta_i)(1 - 3\cos^2\theta_s) + a(B, \delta)\cos\theta_i \sin\theta_i \cos\theta_s \sin\theta_s + \tfrac{1}{2} c(B, \delta) \sin^2\theta_i \sin^2\theta_s] \, , \\
H_{IQ} &= \tfrac{3}{4} E_1 [\tfrac{1}{2}\sin^2\theta_i(1 - 3\cos^2\theta_s) + a(B, \delta)\cos\theta_i \sin\theta_i \cos\theta_s \sin\theta_s - \tfrac{1}{2} c(B, \delta) \sin^2\theta_s(1 + \cos^2\theta_i)] \, , \\
H_{IU} &= \tfrac{3}{4} E_1 [b(B, \delta)\sin\theta_i \cos\theta_s \sin\theta_s - d(B, \delta)\cos\theta_i \sin^2\theta_s] \, , \\
H_{QI} &= \tfrac{3}{4} E_1 [\tfrac{1}{2}\sin^2\theta_s(1 - 3\cos^2\theta_i) + a(B, \delta)\cos\theta_i \sin\theta_i \cos\theta_s \sin\theta_s - \tfrac{1}{2} c(B, \delta) \sin^2\theta_i(1 + \cos^2\theta_s)] \, , \\
H_{QQ} &= \tfrac{3}{4} E_1 [\tfrac{1}{2}\sin^2\theta_s(1 - 3\cos^2\theta_i) + a(B, \delta)\cos\theta_i \sin\theta_i \cos\theta_s \sin\theta_s + c(B, \delta)(1 + \cos^2\theta_i)(1 + \cos^2\theta_s)] \, , \\
H_{QU} &= \tfrac{3}{4} E_1 [b(B, \delta)\sin\theta_i \cos\theta_s \sin\theta_s + d(B, \delta)\cos\theta_i \, (1 + \cos^2\theta_s)] \, , \\
H_{UI} &= \tfrac{3}{4} E_1 [-b(B, \delta)\cos\theta_i \sin\theta_i \sin\theta_s + d(B, \delta)\cos\theta_s \sin^2\theta_i] \, , \\
H_{UQ} &= \tfrac{3}{4} E_1 [-b(B, \delta)\cos\theta_i \sin\theta_i \sin\theta_s - d(B, \delta)\cos\theta_s \, (1 + \cos^2\theta_i)] \, , \\
H_{UU} &= \tfrac{3}{4} E_1 [a(B, \delta)\sin\theta_i \sin\theta_s + 2c(B, \delta)\cos\theta_s \cos\theta_i] \, , \\
H_{VV} &= \tfrac{3}{4} E_3 [\cos\theta_i \cos\theta_s + a(B, \delta)\sin\theta_i \sin\theta_s] \, , \\
H_{IV} &= 0, \qquad H_{QV} = 0, \qquad H_{UV} = 0 \, , \qquad H_{VI} = 0 \, , \qquad H_{VQ} = 0 \, , \qquad H_{VU} = 0 \, ,
\end{aligned} \tag{A3}$$

where E_1, E_2, and E_3 were discussed in § 2.1.1, and the various angular parameters were defined in § 3.1. All of the magnetic effects enter the phase matrix through the functions a, b, c, and d, which are

$$\begin{aligned}
a(B, \delta) &= 2\cos\alpha_1 \cos(\delta - \alpha_1) \, , \\
b(B, \delta) &= 2\cos\alpha_1 \sin(\delta - \alpha_1) \, , \\
c(B, \delta) &= \cos\alpha_2 \cos(2\delta - \alpha_2) \, , \\
d(B, \delta) &= \cos\alpha_2 \sin(2\delta - \alpha_2) \, ,
\end{aligned} \tag{A4}$$

where the angular quantity α_k for $k = 0$, 1, or 2 is defined by

$$\tan\alpha_k = \frac{k g_L e B}{2 m_e c A_{ul}} \, . \tag{A5}$$

Note that in the zero field limit, $\alpha_1 = \alpha_2 = 0$, and $H(\boldsymbol{n}_i, \boldsymbol{n}_s)$ reverts to the phase function for nonmagnetic resonance-line scattering. In the case of unpolarized incident light, only the matrix elements H_{II}, H_{QI}, and H_{UI} will be of interest. At the opposite extreme where the magnetic field strength is extremely large, $\alpha_1 = \alpha_2 = \pi/2$, so $a = b = c = d \rightarrow 0$. The only phase function elements that do not vanish in the large field limit are H_{II}, H_{IQ}, H_{QI}, H_{QQ}, and H_{VV}. If the incident light is unpolarized, then only H_{II} and H_{QI} are needed to compute the polarization of the scattered light.

Here we briefly remind the reader of the restrictions under which equation (A3) is valid. The major assumption is that the frequency and directional redistributions of the scattered light are independent. This is true under the following conditions: (1) coherent scattering for which collisional broadening is negligible, (2) weak magnetic fields such that the Zeeman components are not well separated with respect to their natural widths, and (3) frequencies in the vicinity of the line core.

The final ingredient for calculating the transfer of polarized light in a magnetic medium is the Mueller rotation matrix, $L(\gamma)$. This matrix performs a transformation of the Stokes parameters through a rotation angle of γ about some specified axis, and is needed to insure that the Stokes parameters Q and U for the linear polarization are consistently measured along the observer's axes. The Mueller matrix is

$$L(\gamma) = \begin{pmatrix} 1 & 0 & 0 & 0 \\ 0 & \cos 2\gamma & \sin 2\gamma & 0 \\ 0 & -\sin 2\gamma & \cos 2\gamma & 0 \\ 0 & 0 & 0 & 1 \end{pmatrix}. \tag{A6}$$

To summarize, the polarization from a single scattering event is computed according to the following sequence. (1) Transform the incident Stokes vector via the Mueller matrix to the local coordinate system of the magnetic field, in which the field direction is defined to be the local z-axis. This step is required because equations (A2), (A3), and (A4) are only valid in that coordinate system. (2) Employ the scattering phase function H to determine the polarimetric properties of the light in the coordinate system of the magnetic field. (3) Make another Mueller matrix rotation of the Stokes vector of the scattered light to the coordinate system of the observer. This three-step sequence must be repeated for every scattering event occurring in the circumstellar envelope, and the resultant Stokes vectors must be summed to obtain the net polarimetric properties of the flux as seen by the observer.

REFERENCES

Babel, J., North, P., & Queloz, D. 1995, A&A, 303, 5
Bjorkman, J. E., & Bjorkman, K. S. 1994, ApJ, 436, 818
Bommier, V., Landi Degl'Innocenti, E. L., Leroy, J., & Sahal-Bréchot, S. 1994, Sol. Phys., 154, 231
Bommier, V., Leroy, J.-L., & Sahal-Bréchot, S. 1986, A&A, 156, 90
Borra, E. F., & Landstreet, J. D. 1979, ApJ, 228, 809
Brown, J. C., & McLean, S. 1977, A&A, 57, 141
Cassinelli, J. P. 1982, in Proc. IAU Symp. 99, Wolf-Rayet Stars: Observations, Physics, Evolution, ed. C. W. H. de Loore & A. J. Willis (Dordrecht: Kluwer), 173
Cassinelli, J. P., Nordsieck, K. H., & Murison, M. A. 1987, ApJ, 317, 290
Chandrasekhar, S. 1960, Radiative Transfer (New York: Dover)
Chanmugam, G. 1992, ARA&A, 30, 143
Chevalier, R. A., & Luo, D. 1994, ApJ, 421, 225
Collins, G. W., II. 1989, The Fundamentals of Stellar Astrophysics (New York: Freeman)
Corney, A. 1977, Atomic and Laser Spectroscopy (Oxford: Clarendon)
dos Santos, L. C., Jatenco-Pereira, V., & Opher, R. 1993, ApJ, 410, 732
Dumont, S., Pecker, J. C., Omont, A., & Rees, D. 1977, A&A, 54, 675
Faurobert-Scholl, M. 1992, A&A, 258, 521
———. 1993, A&A, 268, 765
Fox, G. K. 1991, ApJ, 379, 663
Haisch, B., & Schmidt, J. H. M. M. 1996, PASP, 108, 113
Hanle, W. 1923, Naturwissenschaften, 11, 690
Hillier, D. J. 1996, preprint
Höflich, J. C., Wheeler, J. C., Hines, D. C., & Trammell, S. R. 1996, ApJ, 459, 307
House, L. L. 1970, J. Quant. Spectrosc. Radiat. Transfer, 10, 1171
Ignace, R., Cassinelli, J. P., & Nordsieck, K. H. 1997, in ASP Conf. Proc. 120, Luminous Blue Variables: Massive Stars in Transition, ed. A. Nota & H. J. G. L. M. Lamers (San Francisco: Lamers), in press
Jeffery, D. J. 1988, Ph.D. thesis, McMaster Univ.
———. 1989, ApJS, 71, 951
Johns-Krull, C. M., & Valenti, J. A. 1996, ApJ, 459, L95
Kartje, J. F. 1995, ApJ, 452, 565
Lamers, H. J. G. L. M., & Cassinelli, J. P. 1996, in preparation
Landi Degl'Innocenti, E. L. 1990, in Dynamics of Quiescent Prominences, ed. V. Rŭzdja & E. Tandberg-Hanssen (Berlin: Springer), 206
Landstreet, J. D., Barker, P. K., Bohlender, D. A., & Jewison, M. S. 1989, ApJ, 344, 876
Leroy, J.-L. 1985, in Measurements of Solar Vector Magnetic Fields, ed. M. J. Hagyard (NASA Conf. Publ. 2374), 121
Lou, Y., & Rosner, R. 1994, ApJ, 424, 429
McKenna, S. J. 1981, Ph.D. thesis, Ohio State Univ.
———. 1984, Ap&SS, 106, 283
———. 1985, Ap&SS, 108, 31
Mihalas, D. 1978, Stellar Atmospheres (New York: Freeman)
Mitchell, A. C. G., & Zemansky, M. W. 1934, Resonance Radiation and Excited Atoms (New York: Cambridge)
Morton, D. C. 1991, ApJS, 77, 119
Moruzzi, G., & Strumia, F., eds. 1991, The Hanle Effect and Level-Crossing Spectroscopy (New York: Plenum)
Nagendra, K. N. 1988, ApJ, 335, 269
Omont, A., Smith, E., & Cooper, J. 1973, ApJ, 182, 283
Poe, C. H., Friend, D. B., & Cassinelli, J. P. 1989, ApJ, 337, 888
Redman, R. O. 1941, MNRAS, 101, 266
Sahal-Brèchot, S., Malinovsky, M., & Bommier, V. 1986, A&A, 168, 284
Shore, S. N. 1987, AJ, 94, 731
Stenflo, J. O. 1980, A&A, 84, 68
———. 1982, Sol. Phys., 80, 209
———. 1994, Solar Magnetic Fields (Dordrecht: Kluwer)
Stenflo, J. O., & Nagendra, K. N., eds. 1996, Proc. Workshop on Solar Polarization, Sol. Phys., 164,
Stenflo, J. O., & Stenholm, L. 1976, A&A, 46, 69
Weber, E. J., & Davis, L., Jr. 1967, ApJ, 148, 217
Weiskopf, V. 1931, Ann. Phys., 9, 23
Wood, K., & Brown, J. C. 1994a, A&A, 285, 220
———. 1994b, A&A, 291, 202
Wood, K., & Bjorkman, J. E. 1995, ApJ, 443, 348
Wood, K., Bjorkman, J. E., Whitney, B., & Code, A. 1996, ApJ, 461, 847
Whitney, B. A. 1991a, ApJS, 75, 1293
———. 1991b, ApJ, 369, 451
Zanstra, H. 1941a, MNRAS, 101, 250
———. 1941b, MNRAS, 101, 273